Geochemistry, Geophysics, Geosystems®

RESEARCH ARTICLE
10.1029/2024GC012005

Key Points:

- Brittle faulting associated with hot-fluid circulation is described along the Transantarctic Mountains front
- Apatite fission-track ages of 23 Ma reveal a local thermal resetting associated to a paleo-hydrothermal system
- Oblique rifting propagated toward the Transantarctic Mountains front synchronously with offshore faulting

Supporting Information:
Supporting Information may be found in the online version of this article.

Correspondence to:
M. Fioraso,
marco.fioraso@unisi.it

Citation:
Fioraso, M., Olivetti, V., Balsamo, F., Rossetti, F., Zattin, M., & Cornamusini, G. (2025). Cenozoic structurally controlled hydrothermal activity revealed by apatite thermochronology in the Convoy Range (southern Victoria Land, Antarctica). *Geochemistry, Geophysics, Geosystems*, *26*, e2024GC012005. https://doi.org/10.1029/2024GC012005

Received 31 OCT 2024
Accepted 15 MAR 2025

Author Contributions:
Conceptualization: M. Fioraso, V. Olivetti, F. Balsamo, F. Rossetti, M. Zattin, G. Cornamusini
Data curation: M. Fioraso, V. Olivetti, F. Balsamo
Formal analysis: M. Fioraso, F. Rossetti
Funding acquisition: V. Olivetti, F. Balsamo, G. Cornamusini
Investigation: M. Fioraso, V. Olivetti, F. Balsamo
Methodology: M. Fioraso, V. Olivetti, F. Balsamo, F. Rossetti
Project administration: M. Zattin, G. Cornamusini
Resources: V. Olivetti

Cenozoic Structurally Controlled Hydrothermal Activity Revealed by Apatite Thermochronology in the Convoy Range (Southern Victoria Land, Antarctica)

M. Fioraso[1], V. Olivetti[2], F. Balsamo[3], F. Rossetti[4], M. Zattin[2], and G. Cornamusini[1,5]

[1]Department of Physical Sciences, Earth and Environment, University of Siena, Siena, Italy, [2]Department of Geosciences, University of Padova, Padova, Italy, [3]Department of Chemistry, Life Sciences and Environmental Sustainability, University of Parma, Parma, Italy, [4]Department of Science, University of Roma Tre, Roma, Italy, [5]Museo Nazionale dell'Antartide, University of Siena, Siena, Italy

Abstract The Transantarctic Mountains form the longest and highest extensional mountain range on Earth, marking the boundary between the Antarctic craton and the Mesozoic-Cenozoic rifted Ross Sea lithosphere. During the Cenozoic, deep offshore troughs, such as the Terror Rift, developed at the front of the Transantarctic Mountains in response to transtensional dextral kinematics that overprinted an older phase of orthogonal rifting. On land, few direct age constraints of Cenozoic faulting exist, and evidence of fault activity is often inferred from fission track age dating. In this study, we focused on the Convoy Range block in southern Victoria Land, a region with limited field surveys and thermochronological data. We present the results of multiscale structural analysis, geothermometry, and apatite fission-track thermochronology aimed at reconstructing the fault architecture and timing of deformation. The fault pattern is dominated mainly by nearly N-S striking normal faults, with a subordinate system of right-lateral transtensional faults. Brittle deformation is accompanied by diffuse propylitic alteration and carbonatization, providing evidence of hydrothermal fluid-rock interaction in a mesothermal environment (~175–325°C). Fission track ages of fault rocks as young as ~23 Ma are interpreted as local thermal resetting along faults, potentially constraining the age of deformation. These results document a case of structurally controlled hydrothermal fluid flow coeval to Cenozoic transtensional reactivation in Victoria Land, with important implications for the onset of Cenozoic volcanism in the region.

Plain Language Summary Extensional tectonics caused by the prolonged stretching between East and West Antarctica has shaped the landscape of the Transantarctic Mountains. We investigated brittle deformation zones in the granitic Paleozoic basement of the Convoy Range in southern Victoria Land, where evidence of a fossil, structurally controlled hydrothermal activity was identified. The timing of these thermal anomalies in fault zones can be detected using apatite fission-track thermochronology, which resets at temperatures above ~120°C. Our analysis reveals an episode of thermal reset around 23 Ma (early Miocene). Hot fluid circulation altered the granitic basement, leading to the formation of hydrothermal minerals like chlorite, whose chemistry indicates formation temperature ranging ~175–325°C. This heating event overlaps with the tectonic activity in the nearby Terror Rift. Our findings suggest that fluid circulation assisted by Cenozoic faulting within the rifted lithosphere impacted the thermal structure of the coastal escarpments of the Transantarctic Mountains. This work provides insights into possible links between Cenozoic rifting and McMurdo volcanism, mediated by brittle tectonic structures located onshore, offset from the rifting axis.

1. Introduction

High-elevation rift flanks are commonly observed along the borders of passive margins and extensional basins, resulting from the interplay among uplift driven by thermo-mechanical processes, isostatic response (Stern et al., 2005; van der Beek et al., 1994), and surface lowering due to erosion (Braun, 2018; Braun & van der Beek, 2004). Significant research is focused on understanding the long-lasting nature of rift margins (for a review, Wildman et al., 2019), incorporating a range of erosional scenarios, derived from quantitative analysis of surface processes and topographic evolution (Braun, 2018; Gallagher et al., 1998). However, the erosive nature of high-elevation rift flanks limits the effectiveness of techniques used to determine the rates and timing of tectonic activity, particularly during the initial phases of rifting, when the main build-up of topography occurred. Studying syn-rift sedimentary sequences in extensional basins adjacent to uplifted flanks allows for precise constraints on rifting dynamics (e.g., Braun & Beaumont, 1989) and the source-to-sink history. Meanwhile, fault system

Supervision: V. Olivetti, F. Rossetti, G. Cornamusini
Validation: M. Fioraso, V. Olivetti, F. Balsamo
Visualization: M. Fioraso
Writing – original draft: M. Fioraso, V. Olivetti, F. Balsamo
Writing – review & editing: M. Fioraso, V. Olivetti, F. Balsamo, F. Rossetti, M. Zattin, G. Cornamusini

propagation and structurally controlled landscape evolution can be interpreted using low-temperature thermochronology, especially in crystalline basement rocks (Fitzgerald, 1992; Gallagher et al., 1998). Nonetheless, direct constraints on the age of tectonic activity are often lacking.

The age of faulting is typically determined by dating fault rocks, such as pseudotachylytes (e.g., Di Vincenzo et al., 2004, 2013, 2019; Murakami et al., 2006; Zanchetta et al., 2011), or fault-related mineralization, such as carbonate and/or hematite coatings (Ault, 2020; Calzolari et al., 2018; Hansman et al., 2018; McDermott et al., 2021; Nuriel, 2012; Roberts & Holdsworth, 2022; Watanabe, 2008). An alternative approach is to use thermochronological systems to date minerals in the host rocks that were reset by the thermal anomaly due to faulting (Tagami, 2012). Frictional heating is generally confined to the first few centimeters from the fault core, whereas heating by syn-tectonic fluid circulation can impact a much broader portion of the fault damage zone (Tagami, 2019).

Low-temperature apatite and zircon thermochronology is a valuable tool for constraining the timing of structurally controlled fluid migration in paleo-hydrothermal systems, as demonstrated by the fluid-mediated enhanced mobility of chemical species like rare earth elements (REE) (Milesi et al., 2020). Additionally, quantitative analysis of grain age dispersion and confined tracks can be integrated with the architecture and physical properties of the fault zone (Murakami & Tagami, 2004; Yamada et al., 2007; Wölfler et al., 2010). Faulting and fluid flow are closely linked in most tectonic settings. Stress-induced increases in fluid pore pressure help reducing the frictional yield limit, while fracture propagation enhances secondary permeability, providing preferential pathways for fluid circulation. In continental rift systems, hydrothermal circulation is both spatially and temporally associated with deep crustal discontinuities (Brune et al., 2017; Muirhead et al., 2016; Ring et al., 2016; Tagami et al., 1988). Investigating brittle deformation structures that act as pathways for hydrothermal fluids is therefore crucial for understanding rift systems in both space and time (Brune et al., 2023; Pérez-Gussinye et al., 2023).

The Transantarctic Mountains (TAM) represent the western high-elevation rift flank (Fitzgerald, 2002; Lisker & Läufer, 2013; Olivetti et al., 2018) of the West Antarctic Rift System, a ∼600 km wide continental rift, recognized as one of the largest on Earth (Cooper et al., 1991; Elliot, 2013; Jordan et al., 2020; Siddoway, 2008). The TAM are formed by the remnants of thickened lithosphere (Bialas et al., 2007; Tinto et al., 2019) through multiple extension phases since the breakup of Gondwana (Harry et al., 2018; Siddoway, 2008). The landscape of the TAM results from a complex interplay of continental rifting, passive margin uplift, fluvio-glacial erosion driven by global climate variations, and deep Earth processes (Balestrieri et al., 2020; Brenn et al., 2017; Cooper et al., 1991; Faccenna et al., 2008; Fitzgerald, 2002; Levy et al., 2019; Stern et al., 2005; Sugden & Denton, 2004; Sugden & Jamieson, 2018). This landscape evolution occurred during the Cenozoic, coinciding with the onshore propagation of intraplate strike-slip shearing across northern Victoria Land since the Eocene-Oligocene (Di Vincenzo et al., 2004; Rossetti et al., 2006; Salvini et al., 1997). The transtensional stress regime established during this period remains active today (Cianfarra et al., 2022; Dubbini et al., 2010; Vignaroli et al., 2015; Wilson, 1995, 1999; Zanutta et al., 2017).

In this study, we investigate onshore rift propagation in southern Victoria Land, focusing specifically on the Convoy Range block (Figure 1). We integrate a multi-scale structural analysis with petrographic observations and apatite fission-track (AFT) thermochronology. Abrupt variations in age-elevation relationships from fault-orthogonal sampling transects provide the first evidence of early Miocene anomalous, structurally controlled heating events, likely caused by hydrothermal fluid-rock interactions along fault damage zones. Additionally, microanalytical characterization of hydrothermal mineralizations can serve as a supplementary tool for refining thermochronological modeling in fault zones.

2. Geological Background

The roots of the TAM were established during the Neoproterozoic-Early Paleozoic Ross Orogeny convergence phase (Elliot, 2013; Goodge, 2020; Stump, 1995) and are exposed in the basement rocks of Victoria Land (Figure 1). In southern Victoria Land, these basement rocks consist of metasedimentary and metavolcanic sequences of the Wilson Group and Skelton Group (Goodge, 2020), intruded by plutons of the Granite Harbor Intrusive Complex, emplaced during the Ross Orogeny (530–480 Ma; Elliot, 2013). The Granite Harbor Intrusive Complex is composed primarily of granodioritic plutons, locally intruded by pink-colored alkali granites (Irizar Granite, 489.9 ± 4.4 Ma; Rocchi et al., 2009), and mafic to felsic dyke swarms (Rocchi et al., 2009). After the

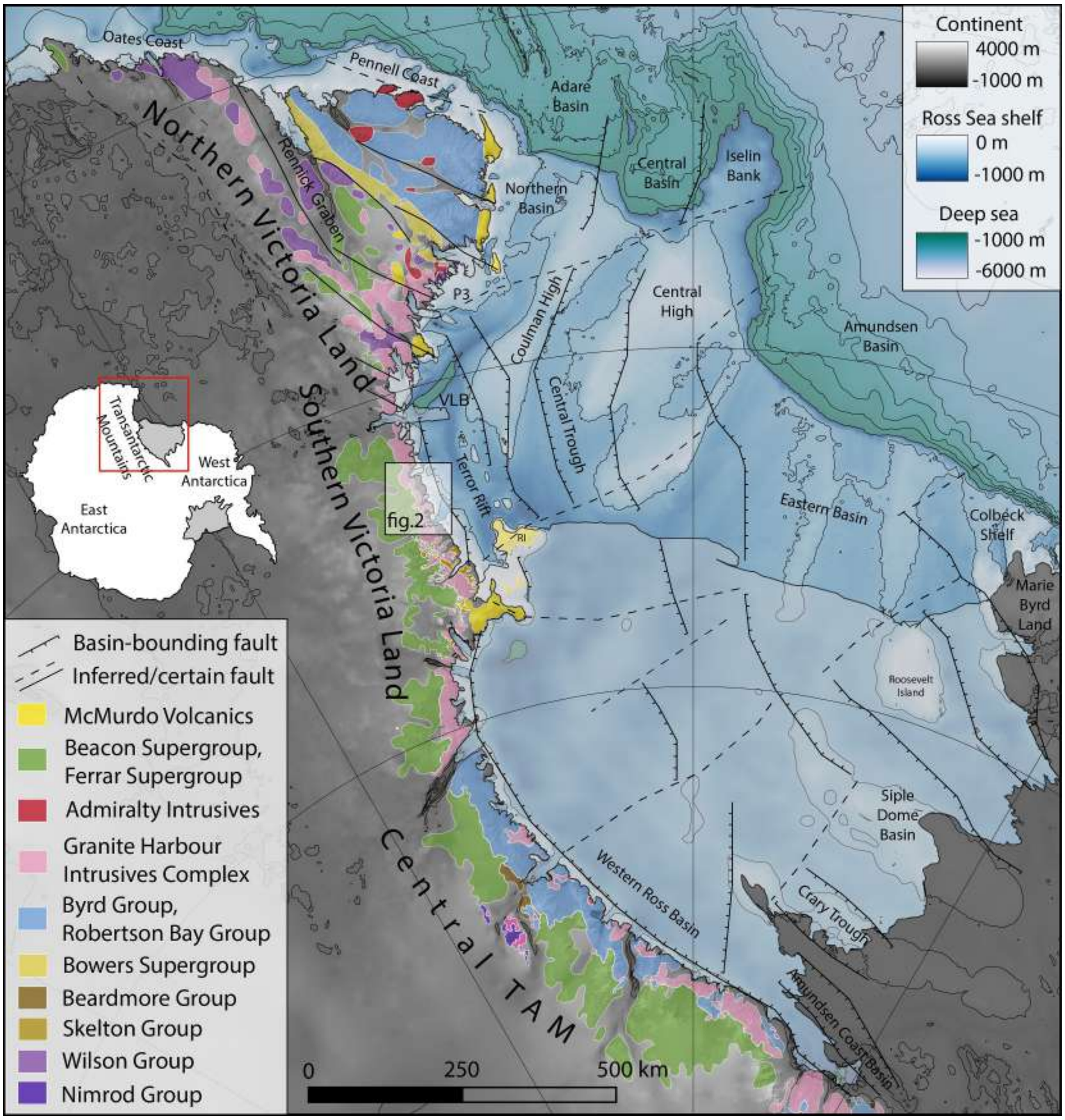

Figure 1. Map of the Transantarctic Mountains and the Ross Sea embayment. The geological framework is adapted from Zurli, Perotti, and Cornamusini (2024). Topography and bathymetry were derived from the BedMachine DEM (Morlighem et al., 2020). Fault data are sourced from Aitken et al. (2023).

cessation of the Ross Orogeny, the orogenic landscape was carved into the Kukri Erosion Surface (Woolfe & Barrett, 1995). This unconformity hosted the deposition of the terrestrial siliciclastic Beacon Supergroup (Cornamusini et al., 2023) in the Transantarctic Basin (Elliot, 1975). This basin was infilled by sediments derived from the Ross Orogen in Devonian times and, later, primarily from the Gondwanide Orogen during the Permian-Triassic (Zurli, Liberato, et al., 2024). During the Early Jurassic (~182.5 Ma), the Ferrar Large Igneous Province was emplaced along the TAM (Elliot et al., 2021b), consisting of: (a) dolerite sills, dikes, and intrusions (Ferrar Dolerite); (b) extrusive flood lavas (Kirkpatrick Basalt); and (c) a variety of volcaniclastic deposits (Elliot and Fleming (2021); Elliot et al., 2021b). Ferrar intrusions are often found in the upper portions of the Granite Harbor plutons, near the Kukri Erosion Surface, or cutting through the Beacon Supergroup sequence (Cox et al., 2012).

As Gondwana fragmented and Australia-Antarctica spreading occurred, the West Antarctic Rift System started along the boundary between the East Antarctic cratonic lithosphere and the West Antarctic lithosphere. The latter was involved in convergence processes with the Paleo-Pacific plate (Jordan et al., 2020). Distributed extension in the West Antarctic Rift System domain and along the TAM is recorded as early as the Cretaceous (~105 Ma;

10.1029/2024GC012005

Bialas et al., 2007; Fitzgerald, 2002; Huerta & Harry, 2007; Siddoway et al., 2004). During the Cenozoic, cooling and strengthening of the West Antarctic lithosphere led to a westward migration of crustal thinning, transitioning to narrow rifting (Wilson & Luyendyk, 2009). E-W motion between East and West Antarctica initiated renewed rifting and ultraslow seafloor spreading, recorded between 43 and 26 Ma in the Adare Basin (Davey et al., 2016). Facing the TAM front, the Ross Sea was compartmentalized into deep graben-like structures (Victoria Land Basin and Northern Basin) separated by transfer zones (Ferraccioli et al., 2009). By the Upper Oligocene (~26 Ma), E-W orthogonal rifting ceased, and deformation in the western Ross Sea transitioned into oblique rifting, which persisted until ~11 Ma (Granot & Dyment, 2018; Sauli et al., 2021; Storti et al., 2007, 2008; Vignaroli et al., 2015). Present-day deformation is consistent with observations of faulting in post-Miocene sediments in the Terror Rift and Quaternary volcanism (Sauli et al., 2021). Active rifting is also accompanied by the emplacement of an alkaline volcanic province (Smellie & Martin, 2021; Smellie & Rocchi, 2021), which extends from the TAM rift flank to the Adare Trough oceanic seafloor (Durkin et al., 2023). Geochemical data indicate that these magmas originated from partial melting of the asthenosphere, enriched by material related to a lithospheric slab subducted along the Gondwana-Pacific convergent margin (Panter et al., 2018). After middle Miocene, volcanism occurred throughout the rifted region, forming onshore volcanic fields, shield volcanoes, stratocones, and scoria cones (Rocchi & Smellie, 2021), as well as offshore volcanic islands and structures in the Victoria Land Basin (Rilling et al., 2009).

2.1. Cenozoic Tectonics

In northern Victoria Land, from the Southern Ocean margin to the Ross Sea, Cenozoic NW-SE dextral intraplate shearing has exploited major crustal discontinuities between terranes that were accreted during the Ross Orogeny (Salvini et al., 1997; Storti et al., 2007). The timing of tectonic activity in this region has been constrained by dating pseudotachylytes in fault rocks, yielding $^{40}Ar/^{39}Ar$ ages that range from 45 to 48 Ma to ~30 Ma (Di Vincenzo et al., 2004, 2013). This tectonic activity was synchronous with the onset of the Meander intrusive magmatism (Rocchi et al., 2002), the exhumation of the TAM (Balestrieri et al., 2020; Fitzgerald, 2002; Prenzel et al., 2018; Rossetti et al., 2003; Storti et al., 2008), and the seafloor spreading of the Adare Trough (Cande & Stock, 2006). The eastern terminations of strike-slip faults along the N-S trending TAM front (Rossetti et al., 2006) partially overlap with transtensional faults bounding the Neogene Terror Rift Basin (Sauli et al., 2021), suggesting a connection in deformation geometry and activity between the intraplate dextral shearing and the Ross Sea rifting (Storti et al., 2007). Onshore, Cenozoic faulting displays an interplay between NW-SE dextral strike-slip faults and normal faults parallel to the TAM front (Sauli et al., 2021; Vignaroli et al., 2015). The timing of faulting is constrained by cross-cutting relationships with the McMurdo volcanic products, extending into the Quaternary (Vignaroli et al., 2015). Present-day active tectonics in this region is further supported by GPS data (Dubbini et al., 2010; Zanutta et al., 2017).

In southern Victoria Land, the TAM front strikes NNW, following inherited Neoproterozoic-Paleozoic crustal anisotropies that have shaped the architecture of the Mesozoic-Cenozoic rifting (Stump, 1995; Wilson, 1995). The structural characteristics of the rift suggest strain partitioning along en-echelon arrays of NNE-to NE-striking normal and oblique dextral slip faults, as well as ENE-striking left-lateral oblique slip faults (Olivetti et al., 2018; Storti et al., 2008; Wilson, 1995, 1999). Although direct evidence of Cenozoic faulting in the granitic basement is limited, the large-scale morphological alignments of glacial valleys and escarpments imply tectonic control during rift-flank formation and erosion (Fitzgerald, 1992; Olivetti et al., 2018; Sugden & Denton, 2004). Onshore, direct age constraints on faulting are scarce but include post-3.9 Ma tectonic activity at Mount Morning, where faults offset a McMurdo dyke (Martin & Cooper, 2010). Offshore, in the Cape Roberts Basin, NNE-striking fault activity is constrained between ~32 and 24 Ma, based on the stratigraphic age of faulted Oligocene sediments (Hamilton et al., 2001). The period of major tectonic activity and subsidence in the Terror Rift is placed between 29 and 13 Ma, as suggested by cross-cutting seismic unconformities (Sauli et al., 2021) and the change in position of the East-West Antarctica Euler pole (Granot & Dyment, 2018). The NNW-striking fault system between the Cape Roberts Basin and the TAM coast is the dominant structural feature in the region, controlling the tectonic uplift of the rift-flank and downfaulting the Paleozoic Beacon Sandstone to depths of ~3 km, as seen in the CRP-3 core (Cape Roberts Science Team, 2000). Thermochronological data from nearly vertical profiles along the TAM further support fault-related exhumation, linking block faulting to enhanced uplift around 50 Ma (Fitzgerald, 1992, 2002).

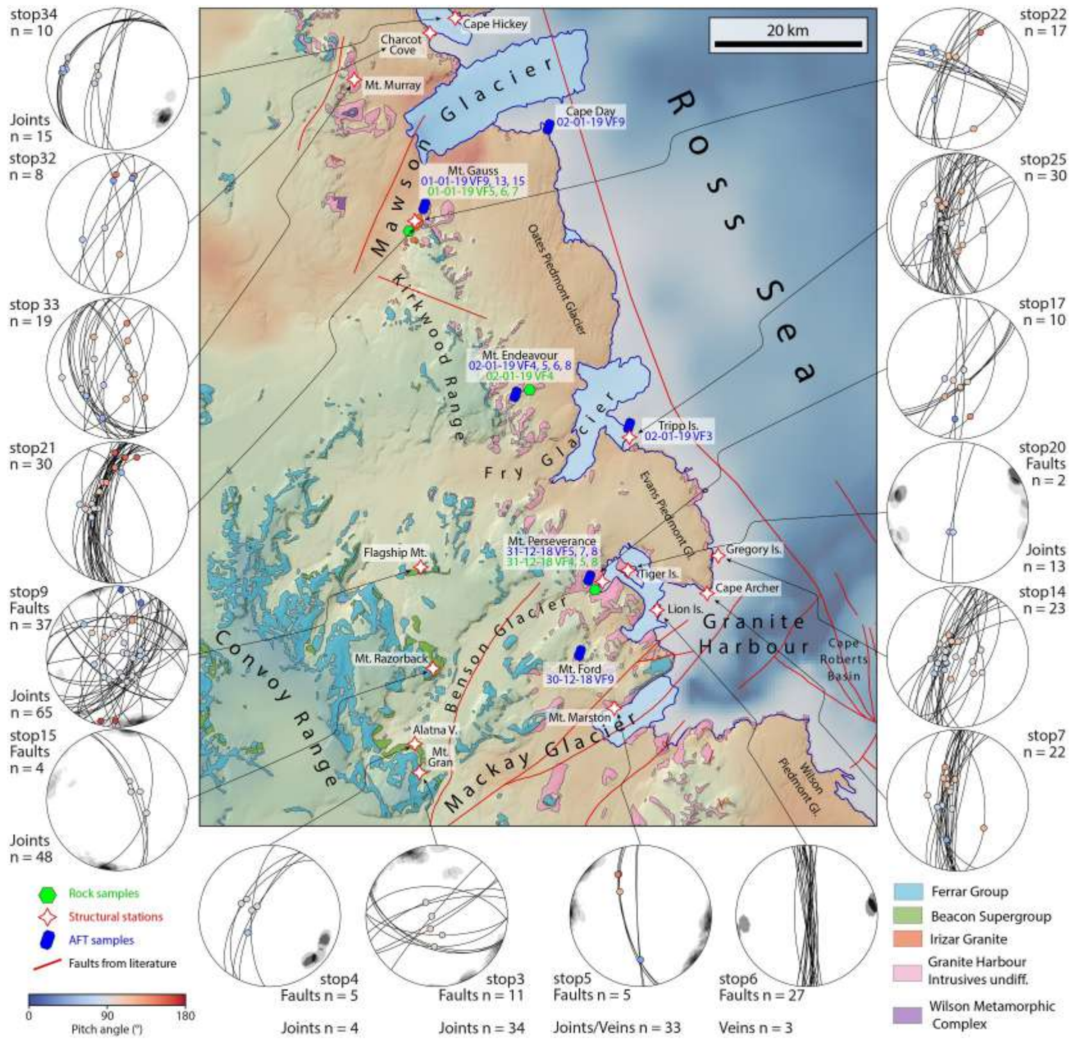

Figure 2. Map of the study area in the Convoy Range sector. Great circles in stereoplots illustrate fault data, while density contours indicate the distribution of vein and extensional fracture poles (all data are shown in lower hemisphere equal-area stereographic projection). Lithologies and faults were redrawn from Cox et al. (2023). Sampling points are marked by green hexagons (rock samples for minero-petrographic analysis) and blue polygons (rock samples for apatite fission-track thermochronology). Topography is sourced from the REMA DEM (Howat et al., 2022).

Structural and fault data for the Convoy Range block in southern Victoria Land remain sparse, with most of the major tectonic features inferred from geological mapping (Capponi et al., 2020, 2024; Cox et al., 2012) (Figure 2). The tectonic framework of the region comprises a set of NNW-SSE striking faults offshore along the TAM front, and a series of transverse NE-SW oriented faults. These NE-SW faults delineate the boundary between the Convoy Range block and adjacent blocks, such as the Dry Valleys block, along key glacial valleys such as the Mackay and Benson glaciers (Cox et al., 2012; Fitzgerald, 1992). Further to the north, similar transverse fault structures are hypothesized beneath the Mawson Glacier, demarcating the separation of the Prince Albert block from the Convoy Range block (Figure 2). Recent detailed structural mapping in the Kirkwood Range has revealed a complex fault pattern, with dip-slip to oblique-slip faults striking in NE-SW, NW-SE, and E-W orientations (Capponi et al., 2024).

2.2. Exhumation Across the Transantarctic Mountains

The simple stratigraphy of the TAM has enabled an effective reconstruction of the rift flank's prolonged exhumation and uplift history, which spans over 100 million years. The onset of exhumation coincides with the beginning of widespread rifting in the Cretaceous (Fitzgerald, 1992, 2002; Miller et al., 2010). Exhumation

10.1029/2024GC012005

processes accelerated significantly between 55 and 50 Ma, in conjunction with the opening of the western Ross Sea basins (Fitzgerald, 1992). A further phase of rapid exhumation is associated with the development of permanent glacial conditions in East Antarctica, around the Eocene-Oligocene boundary (Balestrieri et al., 2020; He et al., 2021; Miller et al., 2010; Olivetti et al., 2018; Prenzel et al., 2018). Despite these periods of increased exhumation, the average exhumation rate remained relatively low at approximately 100 m per million years (Fitzgerald, 2002). More recent exhumation is only detectable in a few areas along the TAM front (Balestrieri et al., 2020; Miller et al., 2010; Olivetti et al., 2018; Storti et al., 2008), indicating that the landscape likely evolved at very low rates after around 15-10 Ma (Sugden & Denton, 2004).

In the Convoy Range block, the available AFT data are limited to 14 samples documented in previous studies (Fitzgerald, 1992; Storti et al., 2008), mostly located in the southernmost region near Granite Harbor (Figure 2). Data collected on the north side of the Mackay Glacier valley in the Granite Harbor area (Fitzgerald, 1992) align with results from the opposite side, around Mt. England (Dry Valleys). Segmentation of crustal blocks along NNW-striking faults, such as the Evans Fault (Gunn & Warren, 1962), and NE-SW faults, may explain observed discrepancies in AFT spatial distributions. In the Kirkwood Range, between the Mt. Creak summit and Tripp Island, fission-track ages (Storti et al., 2008) are similar to the broader TAM exhumation trends, and an exhumed Partial Annealing Zone (PAZ) is inferred to exist at ∼1,100 m.

3. Methods

3.1. Structural Analysis

Structural analysis has been conducted at various scales to elucidate the geometry and kinematic of faults along the studied sector of the TAM front, as well as their relationships with thermochronological data. Structural data from faults and related fractures (including joints and veins) were collected from 22 geo-referenced field sites (Table S1 in Supporting Information S1) during the 33rd and 34th PNRA expeditions (Italian National Research Program in Antarctica). A total of 765 structural measurements were collected (see Table S2 in Supporting Information S1 for details). Fault kinematics were derived mostly from abrasion striae and, subordinately, from slickenfibers (Fe-oxides) which were frequently found on major fault surfaces. Fractures measured in this work mostly refer to mode-1 fractures (i.e., joints). To analyze the fault and fracture populations, contouring and polymodal Gaussian distribution statistics were employed. This approach facilitated the separation of azimuthal and kinematic groups by using the pitch angle measurements (e.g., Storti et al., 2008 and references therein).

Remote sensing analysis was conducted using QGIS 3.34.3 software, incorporating data from the Reference Elevation Model of Antarctica (REMA; Howat et al., 2022), BedMachine DEM (Morlighem et al., 2020), and satellite imagery from the Landsat Image Mosaic of Antarctica (LIMA). This analysis aimed to characterize deformation patterns at both the regional and field site scales. Additionally, geological literature and published geological maps (Capponi et al., 2020, 2024; Cox et al., 2012, 2023) were used to supplement the structural data and enhance the understanding of the geological context.

3.2. Minero-Petrographic Analysis

Rock samples (refer to Table S3 in Supporting Information S1) stored at the National Museum of Antarctica – section of Siena were prepared for microanalytical investigations utilizing various techniques: transmitted-light optical microscopy, scanning electron microscopy (SEM), and electron microprobe analysis (EMPA). Optical microscopy was performed on 12 standard thin sections to identify the mineralogical phases and brittle microstructures present within the samples. The SEM was employed for high-resolution imaging using the backscattered electron (BSE) technique and for analyzing the elemental composition through semiquantitative energy-dispersive spectroscopy (EDS). Imaging and EDS spectra were obtained using a TESCAN SOLARIS dual-beam SEM (Department of Geosciences, UNIPD) and a FEI Quanta 400 SEM (Department of Life Sciences, UNISI). Electron wavelength-dispersive microprobe analyses were conducted using an Oxford Instruments Wave Spectrometer mounted on the TESCAN SOLARIS SEM (Department of Geosciences, UNIPD), and a Jeol JXA-8230 microprobe (CNR-Firenze), both operating at 15 kV and 5 nA. Point analyses with a width of 3 μm were performed to quantitatively determine the elemental composition of chlorite, which was subsequently used in geothermometry calculations executed with WinCCac 1.1 software (Yavuz et al., 2015).

10.1029/2024GC012005

For the chlorite analysis, the semi-empirical model proposed by Bourdelle and Cathelineau (2015) was utilized to predict formation temperatures for low-temperature chlorite (<350°C). This model employs a graphical plot based on silicon (Si) and R^{2+} (divalent cations on octahedral sites), bypassing thermodynamic calculations. It is essential that chlorites be in equilibrium with quartz-bearing rocks ($aSiO_2 = 1$), and contamination from smectite is addressed by excluding analyses where $Na_2O + CaO + K_2O > 0.5$ wt% (Bourdelle, 2021).

The bulk qualitative mineralogy of the rock samples was assessed through X-ray powder diffraction (XRPD) using a PANanalytical diffractometer (Department of Geosciences, UNIPD). This analysis evaluated the presence of mineralogical phases associated with hydrothermal alteration. Additional techniques, including Raman spectroscopy and X-ray fluorescence analysis, were also performed on the rock samples to further characterize their minero-chemical composition. Detailed information regarding these methods and results can be found in the supplementary information (Text S1 and S2 in Supporting Information S1).

3.3. Thermochronology

Apatite fission-track (AFT) thermochronology is a suitable method for detecting the cooling/heating history in the upper crust (3–5 km below the surface) of geological terranes dominated by granitic bedrock, such as those in the TAM region. Fission tracks are linear damage features produced in apatite crystals by the spontaneous nuclear fission decay of ^{238}U, which are retained based on heating and the duration of residence at specific temperatures. In the temperature range between 60°C and 120°C, the sector of the upper crust defined as the Partial Annealing Zone (PAZ) (Gleadow & Fitzgerald, 1987), fission tracks are partially annealed. The density of fission tracks on a polished crystal surface along with other parameters (density of induced tracks, neutron radiation, Zeta factor) provide information on the duration over which tracks accumulate (Hurford, 2019). The length of confined fission tracks (tracks fully contained within the crystal lattice) indicates the duration of stagnation of crystals in the PAZ (Ketcham, 2019).

During progressive exhumation of a crustal section, if a constant relative spacing is maintained between samples, the upper layers pass through the PAZ earlier than the lower layers. The sampling strategy of collecting rocks along vertical profiles allows for the derivation of apparent exhumation rates under certain assumptions (Gleadow & Fitzgerald, 1987). Analyzing the age-elevation relationship (AER) of fission-track samples enables qualitative detection of: (a) changes in exhumation rates (Fitzgerald, 1992; Miller et al., 2010), (b) the presence of tectonic structures (Fitzgerald, 1992; Miller et al., 2010), and (c) heating events (Balestrieri et al., 1997). Quantitative analysis was performed using HeFTy software (Ketcham, 2005). Further details on the thermochronology method can be found in the supplementary information (Text S1 in Supporting Information S1).

In our case study, 13 rock samples collected from the Granite Harbor Intrusive Complex lithologies were obtained along near-vertical profiles (e.g., Mt. Perseverance) and wide, fault-orthogonal transects at Mt. Gauss and Mt. Endeavor. The aim of the thermochronological sampling was to intercept damage zones of Cenozoic transtensive faults and constrain the tectonic activity that shaped the Southern Victoria Land landscape.

4. Structural Data

The collected structural data are presented using stereographic projections from individual sampling locations and are divided into three zones: the Convoy Range in the southwestern portion of the study area, the Granite Harbor in the southeastern coastal portion, and the Mt. Gauss-Mt. Murray region in the northern portion (Figure 2). Significant georeferenced field sites are included, along with outcrop descriptions and remote sensing observations.

4.1. Convoy Range Area

In the Convoy Range, structural data have been collected within the Beacon Sandstones, which predominantly exhibit dip-slip extensional faults, with subordinately occurring strike-slip faults. These faults are oriented along three main directions: NNW-SSE, NNE-SSW, and E-W (Figures 2 and 3). On the eastern side of Mt. Gran (Stop 3), a conjugate system of extensional faults, striking nearly E-W (60°–110°N) has been measured (Figures 2 and 3b). In the same area, joint networks show variable orientations ranging from N-S to E-W (5°–90°N) (Figure 2). On the northern side of Mt. Gran (Stop 4), dip-slip faults are grouped into a single set of NNE-SSW-striking structures (Figure 2). At Mt. Razorback (Stop 15), normal faults predominantly strike NNW-SSE (340°N)

Figure 3. Field sites showing Devonian sandstone outcrops in the Convoy Range. Tectonic structures are illustrated at varying scales of observation: (a) centimetric scale, (b) metric scale, and (c) decametric scale. White solid lines indicate main faults, dashed lines indicate minor shear fractures and joints.

(Figure 2). Conversely, fractures are clustered into two subsets oriented at right angles to each other, with directions along NNE-SSW (0°–45°N) and ESE-WNW (80°–130°N) (Figure 2). At Flagship Mountain, all the previously described structural orientations have been observed. The average orientation is NE-SW (∼40°N) (Figure 2), and extensional fractures are clustered into two subsets, nearly NNW-SSE (310°–360°N) and ENE-WSW (60°–90°N), similar to those at Mt. Razorback (Figure 2).

At the Mt. Gran and Alatna Valley outcrops, millimeter-to meter-scale dip-slip offsets have been observed (Figures 3a–3c). The faults are arranged in conjugate sets. Polished fault planes exhibit a weathered reddish coating (Figure 3b), but there is no evidence of significant fault breccias or cataclasites. While brittle deformation in this area is frequent and pervasive, there is no indication of major down-faulting, as would be expected at the TAM front (Fitzgerald, 1992).

4.2. Granite Harbor Area

In the Granite Harbor sector, from the Mackay Glacier to the Fry Glacier, the Granite Harbor Intrusive rocks are intersected by a set of faults arranged into two subsets. The first subset is oriented N-S (340°–30°N) and is visible at Stops 5, 6, 7, 14, 17, 20, and 25. The second subset is oriented NE-SW (30°–50° N), visible at Stops 14, 17, and 25 (Figure 2). Veins (Figure 2) at Stops 6 and 20 exhibit the same orientation as the fault zones (N-S), whilst at Stop 5, veins and extensional fractures show an average NE-SW orientation consistent with a right lateral transtensive kinematics inferred on fault planes.

The southern wall of Mt. Perseverance, facing the Benson Glacier, reveals the presence of two fault subsets identified through remote sensing analysis (Figure 4a) and field observations (Figures 4c and 4d). The southern escarpment of Mt. Perseverance consists of a ∼4 km-wide band of distributed sub-vertical and predominantly dip-slip faults, oriented N-S (Figure 4a). On the southeast wall, the NE-SW oriented fault set is highlighted by selective erosion on fault plane surfaces, creating a series of triangular facets (Figure 4a). Centimeter-to meter-scale dip-slip offsets are evident in outcrops along fault planes marked by a reddish altered coating (Figure 4c). A

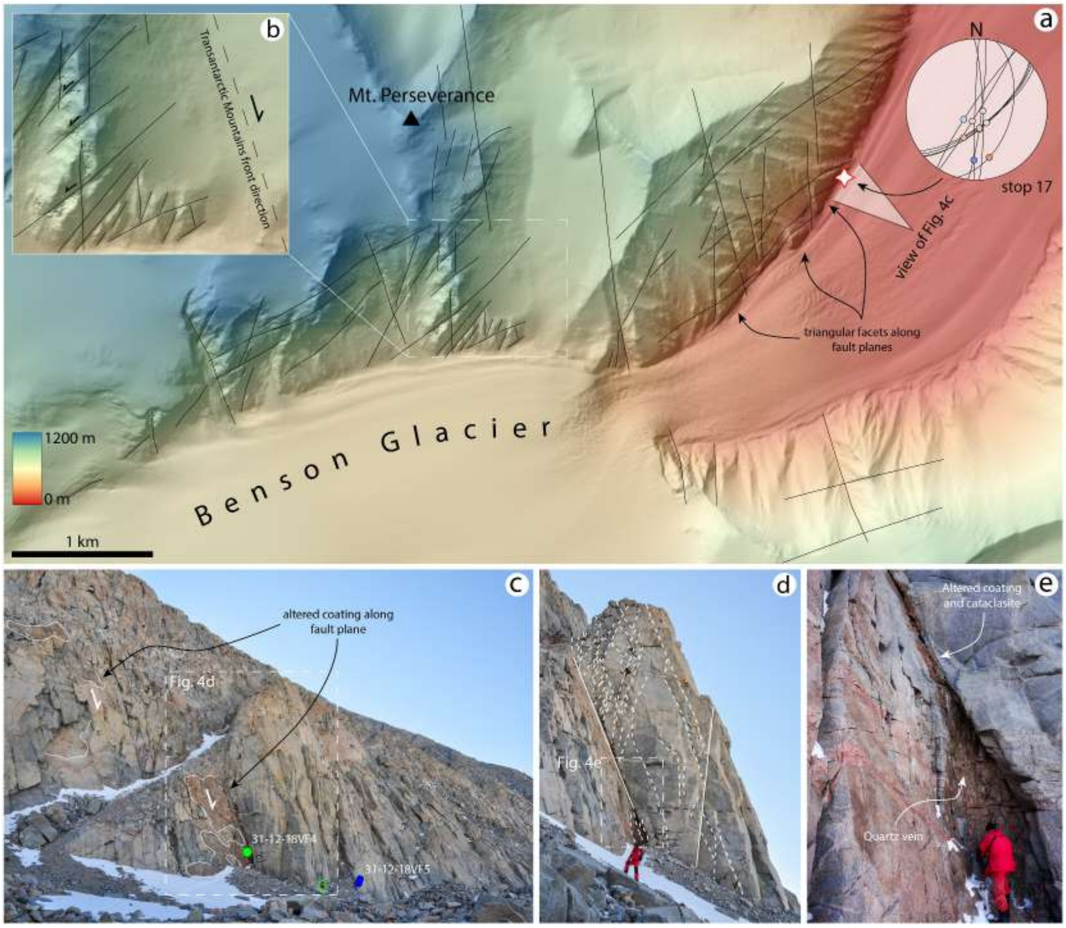

Figure 4. The Mt. Perseverance study area. (a) Tectonic lineaments (black solid lines) detected by remote sensing near sampling locations. (b) The inferred sense of motion is illustrated by offset ridges, which are cut by several parallel structures arranged en-echelon with the trend of the TAM front. The northern wall of Benson Glacier reveals multiple fault planes shown by polished surfaces, reddish by alteration of fault rocks (c, d, e). White solid lines indicate main faults, dashed lines indicate minor shear fractures and joints. The uninterpreted figure is shown as Figure S1 in Supporting Information S1.

subvertical vein set filled with quartz, calcite, and chlorite, as well as millimeter-sized blackish seams and cataclasite, is coherent with the extensional stress field (vertical σ_1 axis) which generated the normal fault at Stop17 (Figure 4e). Strike-slip offsets can be inferred from dissected ridges (Figure 4b), along a shear zone consistent with the partitioning of oblique-slip deformation.

4.3. Mt. Gauss and Mt. Murray Area (Mawson Glacier)

The structural architecture of the Mt. Gauss area (Stops 21 and 22) includes fault zones oriented along two main directions: NNE-SSW (0°–40°N) and WNW-ESE (280°–305°N) (Figure 2). In the Mt. Murray sector, on the northern side of Mawson Glacier (Stops 32, 33, and 34), faults exhibiting normal kinematics strike from NNW-SSE to NW-SW (Figure 2). Additional structural data from Mt. Murray (Figure S3 in Supporting Information S1) reveal the presence of a fault zone striking NE-SW (Stops 11–2017, 25–2017, and 28–2017) and ENE-WSW (Stop 29–2017). The orientation of fracture networks (Figure S3 in Supporting Information S1) is consistent with the fault data.

At Mt. Gauss, a breccia pipe (Stop 21, Figures 5a and 5b), ~0.5–1.5 m wide, and Ross post-collisional Vegetation Lamprophyre dykes (Rocchi et al., 2009; see Table S4 in Supporting Information S1) (crosscut the Irizar Granite (Figure S2 in Supporting Information S1). The breccia pipe primarily consists of angular fragments of Irizar granite, along with subordinate fragments of meta-sediments, meta-rhyolites, and other metamorphic basement materials, indicating the presence of the Wilson Metamorphic Complex and Johnnie Walker Formation

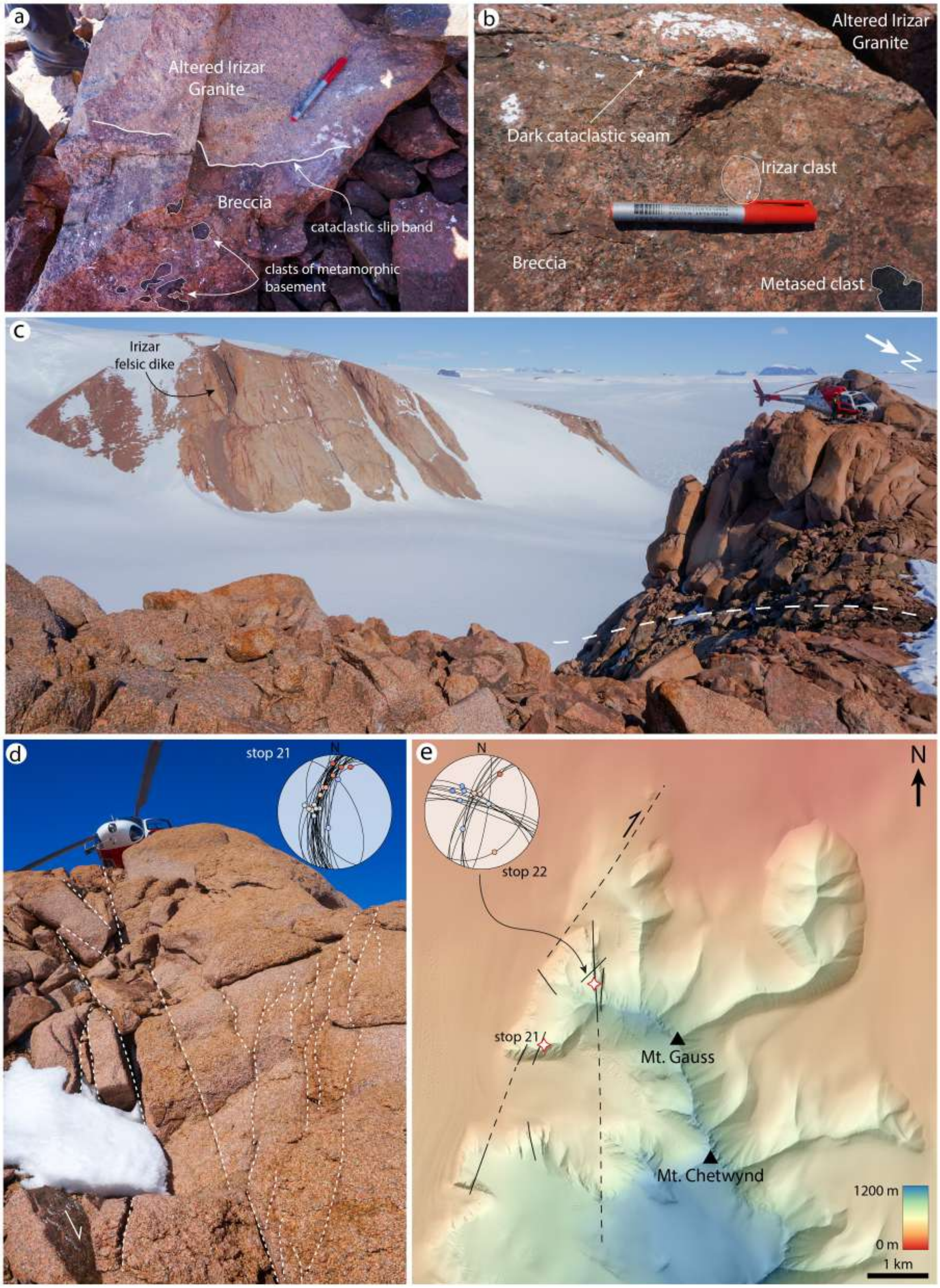

Figure 5. (a–b) The Mt. Gauss site where breccia within the Irizar Granite has been found. (c) A panoramic view to the south from Stop 21, where the Irizar Granite is cut by a felsic Irizar dike, as noted in Rocchi et al. (2009), the inferred fault is shown in white dashed lines. (d) Fault zone observed at Stop 21; dashed lines indicate minor shear fractures and joints. (e) Map of Mt. Gauss showing main faults that intersect sampling sites; solid lines indicate certain faults, dashed lines indicate inferred faults.

(Tessensohn et al., 1992) beneath the Irizar Granite plutons. Sharp contacts between the pipe and the host rock have been reactivated by faulting, as highlighted by a millimeter-sized dark cataclasite vein at Stop 21 (Figure 5a). The entire western ridge (Stop 22) of Mt. Gauss is intersected by faults, spaced several hundred meters apart, striking WNW-ESE, similar to a fault zone described by Capponi et al. (2020) south of Mt. Gauss.

Glacial morphologies in the Mawson Glacier area are significantly influenced by structural elements. The northern side of the glacier follows the fault zone that extends from the base of Mt. Murray to Charcot Cove and Cape Hickey (Figure S3 in Supporting Information S1), while the southern side aligns with the deformation pattern observed at the Mt. Gauss field sites (Figures 5d and 5e). The ∼70° clockwise rotation of the glacial outlet axis coherently reflects the intersection of two distinct deformation patterns, from N-S to ENE-WSW.

4.4. Fault Analysis

Coastal mountain ridge escarpments, extending from Mt. Murray to Granite Harbor, are morphologically developed along a NNW-SSE orientation, influenced by rift flank exhumation on a regional scale and faulting associated with the Victoria Land Basin (see Sauli et al., 2021, and references therein). In contrast, the glacial valleys dissecting the coastal ranges and piedmont plains are structurally controlled by: (a) N-S striking fault zones (e.g., lineaments across Mt. Perseverance, Mt. Endeavor, and Tripp Island in Figure 6) and (b) NE-SW striking fault zones (e.g., structures bounding the Mackay Glacier) as suggested in the literature (Figures 2 and 6). Mt. Perseverance is the best location to observe the interaction between these two main deformation trends. The N-S trend can be traced continuously for more than 15–20 km using remote sensing (Figure 6). The NE-SW trend is well-constrained by morphological evidence on the escarpments (Figure 4a). Just south of Mt. Perseverance, the Benson Glacier divides into two branches, following the deformation framework (Figure 6). Predominantly dip-slip NE-SW and ENE-WSW striking faults are arranged in en-echelon arrays at a 45° angle to the TAM front, consistent with the partitioning of oblique rifting.

Collectively, 266 kinematic indicators (striae) were collected by measuring the pitch of abrasion striae and slickenfibers on polished fault surfaces. All faults in the four sectors, analyzed through pole contouring and Gaussian model distribution, exhibit slip pitch angles ranging from 0° to 180°, with best-fit lines suggesting normal to transtensive and purely transcurrent faults across the different investigated sectors. In the northern sector, the component of strike-slip deformation is dominant along NE-trending faults, as confirmed by the investigated sites (Figure 6). In sector A (Mt. Murray), the main fault zone parallel to Mawson Glacier, striking from N-S to ENE-WSW, shows offsets primarily associated with dip-slip kinematics (65% of fault planes measured), with minor dextral (21%) and sinistral (15%) strike-slip components. In sector B (Mt. Gauss), NNE-SSW striking faults display a slip angle distribution centered around ∼90°, indicating pure dip-slip normal kinematics with a minor dextral strike-slip component. In sector C (Granite Harbor Intrusives), most fault planes striking N-S are clustered within a slip angle range of 60°–120°, which is consistent with the kinematics measured in sector D (Convoy Range), suggesting a normal kinematic regime.

5. Microstructural Observations

We present the microstructural features associated with rock deformation and mineralization along fault zones. Samples were collected from: (a) the Mt. Endeavor ridge along one of the faults forming the shear zone between the Kirkwood Range and Tripp Island; (b) the western ridge of Mt. Gauss (Figure 5); and (c) the base of Mt. Perseverance (Figure 4).

5.1. Mt. Endeavor Fault Rock

In Figure 7, a granodiorite sample (02-01-19VF4), attributed to the Larsen Granodiorite unit (Capponi et al., 2020) from Mt. Endeavor, shows evidence of shear zones visible both in hand-specimens and at the microscale (Figures 7a and 7b). The host rock is a granitic rock made by equigranular crystals of plagioclase, biotite, amphibole and large K-feldspar crystals (up to ∼10 cm). At the hand sample scale offsets along K-feldspar grains are visible. Dark seams characterized by grain-size reduction are bounded by sharp surfaces (Figure 7b). Aggregates of fine-grained quartz, enveloped by matrix-filled shear fractures, are evident near the fault core (Figure 7b). The fault core consists of large angular quartz crystals dispersed within a finer matrix of biotite, K-feldspar, and plagioclase (albite) and amphibole (Figure 7b). Small ∼10 μm zircons and apatite crystals have been identified through SEM analysis. No chlorite or calcite has been found in these faulted rocks. The rock is

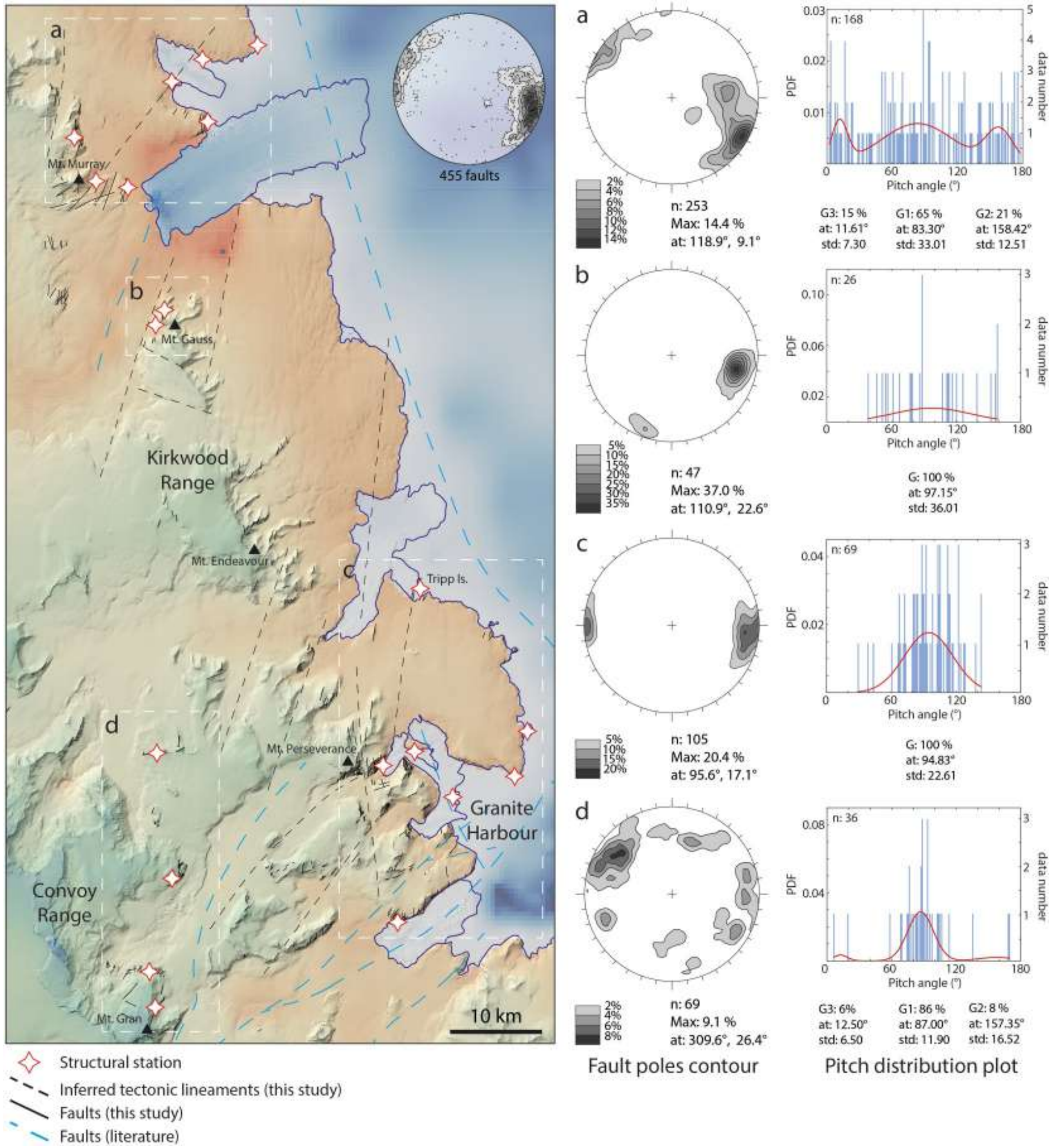

Figure 6. Statistical analysis of fault populations in the Convoy Range block and Mt. Murray sector, utilizing fault pole contour and pitch Gaussian polymodal distribution plots. Sectors include: (a) Mt. Murray, (b) Mt. Gauss, (c) Granite Harbor, and (d) Convoy Range. Faults referenced in the literature are taken from Capponi et al. (2020, 2024), Cox et al. (2023), and Fitzgerald (1992). Additional faults are delineated using remote sensing techniques. The uninterpreted map is shown in Figure S4 in Supporting Information S1.

overprinted by a set of fractures filled with quartz and biotite are oriented in accordance with the dextral shear sense (Figure 7a).

5.2. Mt. Gauss and Mt. Perseverance Hydrothermal Alteration

Propylitic alteration has been documented at Mt. Gauss within and around the fault and the breccia pipe (Stop 21) and at Mt. Perseverance (Stop 17). The breccia at Mt. Gauss is chaotic, with clasts generally exhibiting an angular shape and a fine-grained matrix of quartz, feldspar, and chlorite is recognized (Figures 8a, 8b, and 9a). Pseudomorphic replacement of biotite by chlorite and subordinate anatase is commonly observed (Figures 8b, 8d, 8f and S5 in Supporting Information S1). In the breccia, apatite crystals are frequently found as inclusion in biotite laths (Figure 8f). The breccia is also cut by calcite-quartz-chlorite veins (Figures 8b–8e). In the cataclasite (Figures 9b–9d) and in the partially replaced biotite of the Irizar host rock (Figure 9c), we found aggregates of

10.1029/2024GC012005

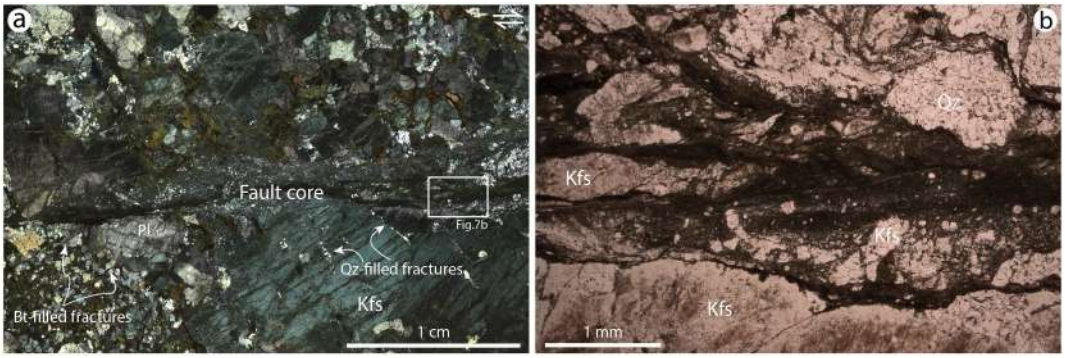

Figure 7. Mt. Endeavor 02-01-19 VF4 fault rock sample. (a) Scanned thin section imaged under cross-polarized light. (b) Parallel-polarized light image of the fault core. Abbreviations: Bt – Biotite, Kfs – Potassium feldspar, Pl – Plagioclase, Qz – Quartz.

microcrystals of (Ce)-bastnäesite (Figure S6 in Supporting Information S1). Large clasts of metasedimentary rocks in the breccia pipe (Figure 8c) display a preserved primary layering (bedding). The protolith consists of fine-grained sandstone/siltstone composed of quartz, plagioclase, and K-feldspar grains, which have been partially recrystallized. Extensional fractures are filled with biotite, which is partially replaced by chlorite (Figure 8d). As a result of pervasive fluid circulation, the undeformed Irizar Granite host rock exhibits significant alteration through sericitization, chloritization, and carbonate (calcite and bastnäesite) precipitation.

On the southern wall of Mt. Perseverance, evidence of hydrothermal fluid circulation is documented along the entire southern cliff. At Stop 19, XRPD qualitative analysis of a granodiorite sample highlights the presence of

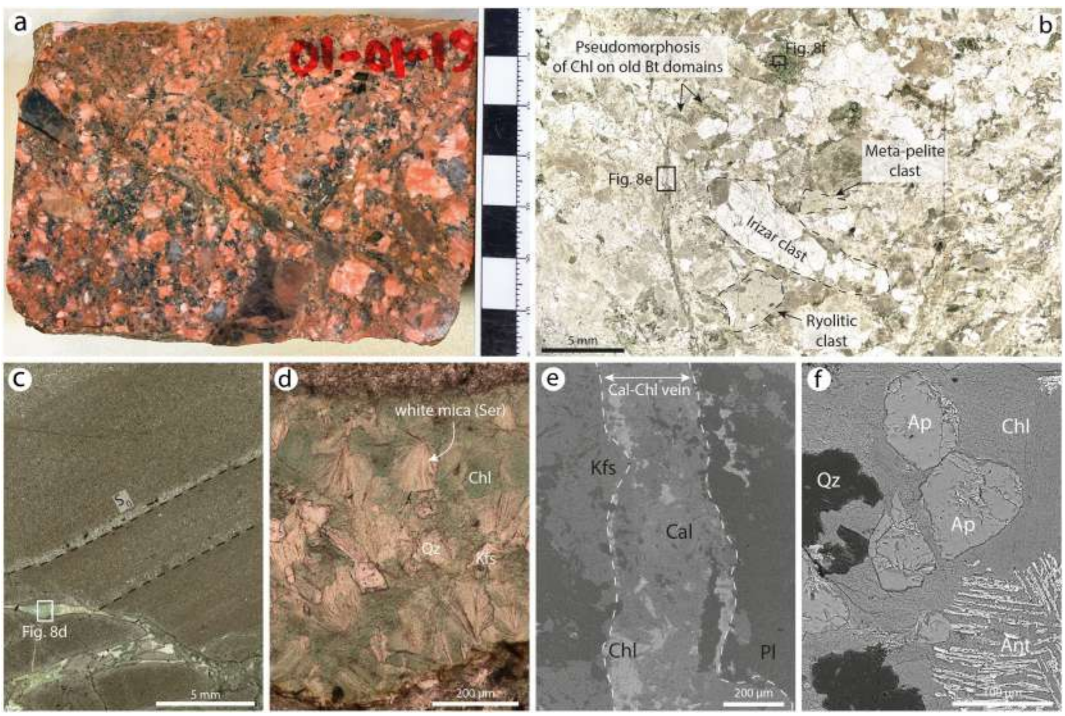

Figure 8. (a) Hand specimen of Mt. Gauss breccia, sample 01-01-19VF5. Scanned thin sections of (b) the breccia and (c) a metasedimentary clast (S_0 is marked by dashed lines). (d) Micropicture (Parallel-polarized light) showing a quartz-chlorite vein cutting across a metasedimentary clast. BSE images depict (e) a calcite-chlorite vein intersecting the breccia and (f) chlorite-anatase pseudomorphosis on a biotite domain where fragments of apatite crystals are cut by chlorite. Abbreviations: Ant – Anatase, Ap – Apatite, Bt – Biotite, Cal – Calcite, Chl -Chlorite, Kfs – Potassium feldspar, Pl – Plagioclase, Qz – Quartz, Ser – Sericite.

10.1029/2024GC012005

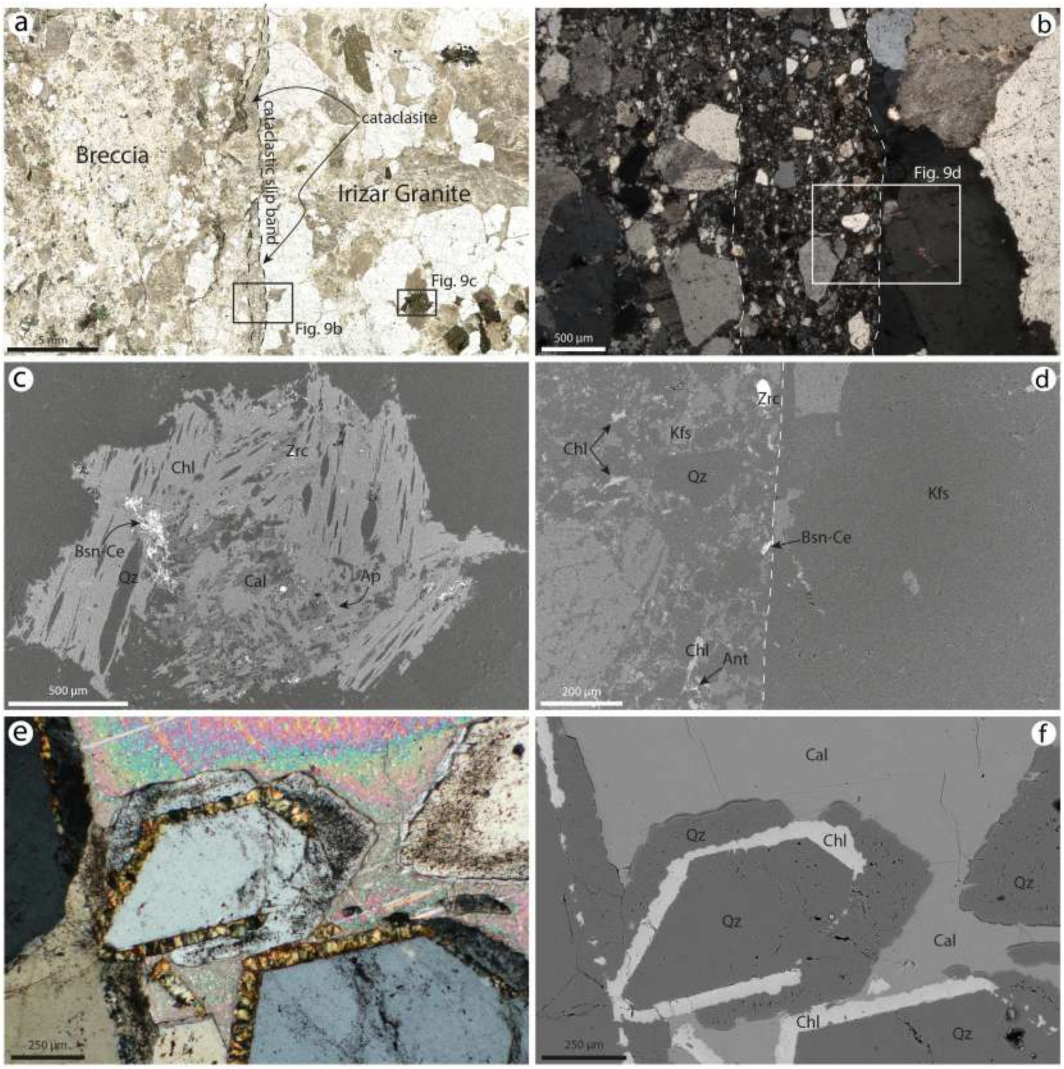

Figure 9. Scanned thin section showing the contact between the breccia and the Irizar Granite host rock, sample 01-01-19VF6. (b) Micropicture (Cross-polarized light) of the cataclastic band. (c) BSE image of the altered biotite crystal within the host rock. (d) BSE image showing the contact between the breccia and host rock, highlighting chlorite, anatase, and (Ce)-bastnäesite. (e) Micropicture (Cross-polarized light) and (f) BSE imaging of a vein from Mt. Perseverance (sample 31-12-18VF4) showing the vein filling assemblage made of quartz, chlorite, and calcite. Abbreviations: Ant – Anatase, Bsn-Ce – (Ce)-Bastnäesite, Cal – Calcite, Chl – Chlorite, Kfs – Potassium feldspar, Qz – Quartz, Zrc – Zircon.

calcite and chlorite (chamosite and clinochlore) (Table S5 in Supporting Information S1). At the base of the cliff (Stop 17), a cataclastic granodiorite sample (31-12-18 VF4) provided the same assemblage of calcite and chlorite (chamosite and clinochlore). In contrast, a sample of undeformed granodiorite collected 20 m far from the faut damage zone (sample 31-12-18 VF5) is altered only by secondary chlorite (Figure S7 in Supporting Information S1). Along the fault zone (Figures 4d and 4e), a ∼2 cm-thick vein filled with large euhedral calcite-quartz crystals associated with chlorite was found (Figures 9e and 9f).

5.3. Chlorite Geothermometry

The environmental temperature of fluid-rock interaction was estimated through WDS (Table S6 in Supporting Information S1) and EMPA (Table S7 in Supporting Information S1) on chlorite crystals from Mt. Gauss and Mt. Perseverance (samples 01-01-19VF5 and 31-12-18VF4). The temperatures, graphically estimated (Bourdelle & Cathelineau, 2015), are organized into two distinct groups close to the Clinochlore/Daphnite composition (Figure S8 in Supporting Information S1). Chlorites from Mt. Gauss are closely clustered, indicating formation

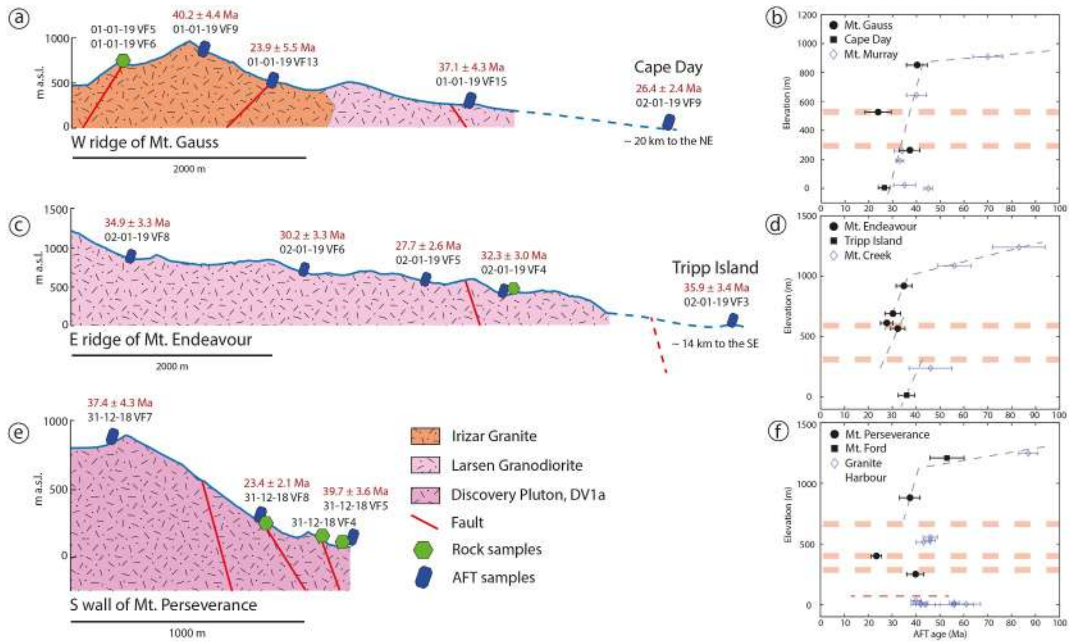

Figure 10. Topographic profiles and apatite fission-track AER for (a, b) Mt. Gauss, (c, d) Mt. Endeavor, and (e, f) Mt. Perseverance. In the age-elevation relationship plots, black symbols represent data collected in this study, while blue diamonds indicate literature data (Fitzgerald, 1992; Guzzo et al., 2019; Storti et al., 2008). Dashed transparent red lines delineate fault zones.

temperatures between 250 and 325°C, whereas chlorites from Mt. Perseverance is more widely distributed in composition, suggesting formation temperatures between 175 and 325°C.

6. Thermochronology Results

In our study of the Convoy Range block, 13 rock samples were collected from Granite Harbor Intrusive Complex lithologies (Irizar Granite, Larsen Granodiorite, Discovery Pluton granite) and analyzed using the fission-track method. Fission-track and counting data are provided in the supplementary information (Tables S8 and S9 in Supporting Information S1). Additional samples collected from Devonian sandstone and heavily deformed fault rocks showed limited recovery of apatite grains. Sampling was performed along two orthogonal transects to the chain: one from Mt. Gauss to Cape Day and the other from Endeavor to Tripp Island (Figure 2). A steep, near-vertical wall in the Granite Harbor sector was also sampled to intercept fault zones observed through remote sensing.

The first transect extends approximately 4 km in the NNE direction across the western ridge of Mt. Gauss (Figure 10a), where three samples were collected at elevations ranging from 250 to 850 m. The AFT ages increase slightly from 37.1 ± 4.3 Ma to 40.2 ± 4.4 Ma, showing ages and AER that are consistent with those from Mt. Murray on the opposite side of Mawson Glacier (Figure 10b). At mid-elevation (527 m), a sample with an age of 23.9 ± 5.5 Ma is anomalously young compared to the trend of the AER and the regional age distribution, which defines the supposed exhumation rate for this TAM sector. Approximately 20 km to the NE, at Cape Day (Figures 2 and 10a), a sample dated at 26.4 ± 2.4 Ma was found at sea level, which aligns with the AER for Mt. Gauss (Figure 10b).

Along the second transect, which is approximately 5 km long and E-W oriented across the eastern ridge of Mt. Endeavor (Figure 10c), four samples were collected at elevations ranging from 560 to 920 m. The AFT ages from the base of the profile are as follows: 32.3 ± 3.0 Ma, 27.7 ± 2.6 Ma, 30.2 ± 3.3 Ma, and 34.9 ± 3.3 Ma. These ages are younger than those reported in the literature (Storti et al., 2008) for Mt. Creak, but are similar to ages found on Mt. Gauss. The age trend decreases from the top of the profile for the highest three samples, while the lower sample and the Tripp Island sample show slightly older ages, following the same AER trend. The transect

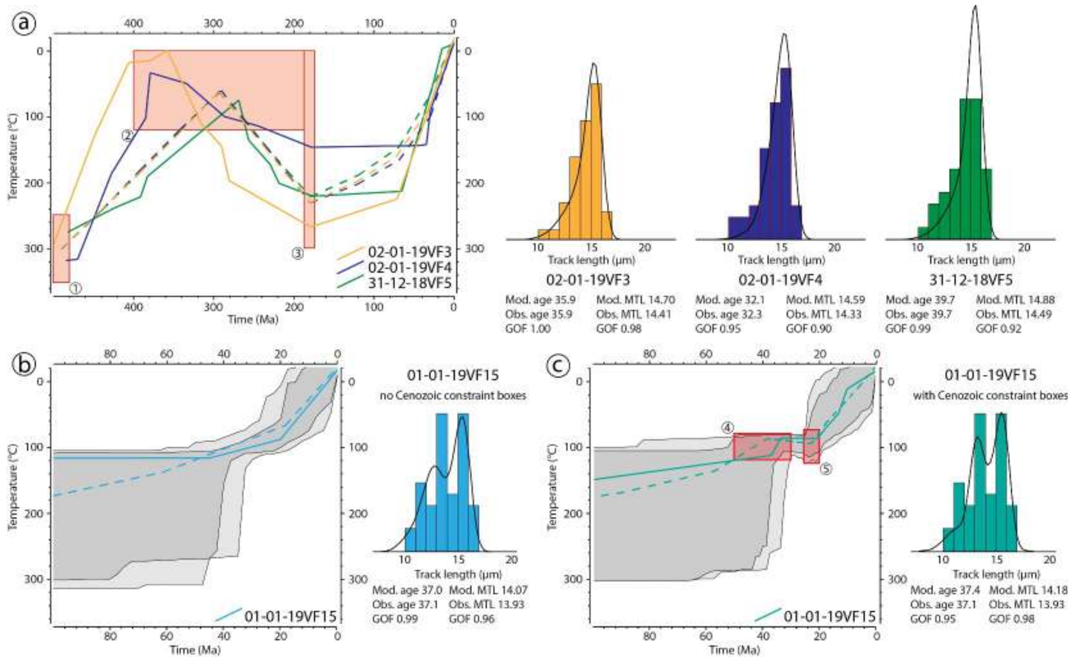

Figure 11. Thermal evolution of samples modeled using HeFTy software (Ketcham, 2005). (a) Time-temperature best fit paths (solid lines) and weighted mean paths (dashed lines) for samples 02-01-19VF3, 02-01-19VF4 and 31-12-18VF5. The last 100 Myr of thermal evolution of sample 01-01-19VF15 without (b) and with (c) constraint boxes in the Cenozoic to test the hydrothermal reheating hypothesis. Full time-temperature paths are shown in Figures S9 and S10 in Supporting Information S1.

intersects a remotely inferred N-S fault zone extending from Mt. Perseverance into the Granite Harbor sector (Figure 6).

The last profile, located on the southern wall of Mt. Perseverance (Figure 10e), is approximately 1 km long and SE oriented, spanning elevations between 250 and 880 m. The lowermost sample yielded an age of 39.7 Ma, consistent with literature data for the same elevation within the same sector. The uppermost sample is slightly younger but remains consistent with the lowermost age. The local AER, combined with literature data, reveals a trend similar to the regional AER, whereas an anomalously young sample located at 400 m above sea level is dated at 23.4 ± 2.1 Ma. This sample originates from a NE-SW striking fault zone detected through remote imaging and analysis. Samples dated at 39.7 ± 3.6 Ma and 37.4 ± 4.3 Ma are respectively found at the bottom and top of the profile. Ages reported in the literature (Fitzgerald, 1992) near the coast are older, consistent with the structure observed on the opposite side of the Mackay Glacier.

Numerical modeling using HeFTy software enables quantitative reconstruction of the thermal histories of samples based on observed data (grain ages, Dpar length, confined track length) and prior constraints chosen from external data. Reconstructions of the final cooling phase are influenced by older geological events, which should be considered in addition to simple interpretations of AER (see Prenzel et al., 2013). We established three time-temperature constraint boxes (Figure 11a): (a) a Cambrian magmatic cooling for the basement rocks of Granite Harbor Intrusive Complex; (b) residence at near-surface temperature during Beacon sandstone deposition, variable in function of the distance from Kukri Erosion Surface; and (c) the reheating caused by the emplacement of the Ferrar Large Igneous Province.

For the three samples, 31-12-18VF5 (at the base of Mt. Perseverance), 02-01-19VF3 (on Tripp Island), and 02-01-19VF4 (at the base of the Mt. Endeavor profiles), the thermal histories (Figure 10a) align well with the observed data. The observed ages and mean track lengths (MTL) are respectively: 39.7 ± 3.6 Ma and 14.49 ± 1.50 μm ($n = 44$); 35.9 ± 3.4 Ma and 14.41 ± 1.33 μm ($n = 48$), 32.3 ± 3.0 Ma and 14.33 ± 1.43 μm ($n = 45$). Long MTL values as in these samples are consistent with a short time over track annealing occurred at the PAZ level, implying an accelerated exhumation synchronous to observed ages around the Eocene-Oligocene boundary.

Thermal modeling of the lowermost sample from Mt. Gauss (01-01-19VF15), with an MTL of 13.93 ± 1.61 ($n = 45$), is complicated by the presence of a double peak in the confined track distribution (Figures 11b and 11c). We run a model with the same constraint boxes already used in previous modeling runs (Figure 11b), and a model with two additional constraint boxes (Figure 11c, see boxes 4 and 5) trying to better reproduce a short cooling/exhumation phase followed by a reheating between 25 and 20 Ma. The thermal history allowed for partial annealing of the confined tracks, producing a negative shift in the secondary peak of the Gaussian distribution. However, the reheating did not sufficiently thermally reset the sample or decrease the AFT age.

7. Discussion

7.1. Tectonic Scenario

The Cenozoic structural pattern of Southern Victoria Land is dominated by en-echelon fault arrays, oriented obliquely to the TAM front (Wilson, 1995). These fault arrays accommodate the regional stress regime through partitioned dip-slip, oblique-slip, and strike-slip faults. In the Dry Valleys, the predominant NE-to-ENE striking faults are mostly dip-slip, while the NNE striking faults exhibit a dextral oblique-slip component (Wilson, 1995). This observation aligns with Riedel-type fracture arrays that trend obliquely to the TAM front. Further south, the structural framework of the TAM front is dissected by E-W and ESE-WNW lineaments, which form the Discovery accommodation zone. However, local subsidiary faults still follow the trends of Riedel-type fractures (Olivetti et al., 2018; Wilson, 1999). In the Prince Albert block, normal and strike-slip synthetic shears are oriented NNE to NE, whereas strike-slip antithetic shear faults are oriented ENE (Storti et al., 2008). Our new data for the Convoy Range block indicate a dominance of N-S to NE-SW faults, primarily dip-slip and right-lateral oblique-slip (Figure 6). Local variations in structural trends are attributed to the reactivation of inherited Paleozoic lineaments and segmentation of the TAM front, as observed in the Cape Roberts Basin, which is located just offshore of the Mackay Glacier (Hamilton et al., 2001). In the Convoy Range sector, fracture orientations may be influenced by the preexistence of tectonic structures coeval with the Ferrar sills emplacement and an Early Jurassic tensile stress field. Nevertheless, the investigation of pre-Cenozoic deformation is not univocal considering that families of faults within the Beacon sandstone sequences are oriented coherently with the stress field generally observed along the TAM front (e.g., Vignaroli et al., 2015, and references therein).

The consistent deformation patterns and landscape morphologies throughout southern Victoria Land suggest that faulting occurs coevally along fault arrays striking at oblique angles to the TAM front. Considering the mechanical consistency of synthetic and antithetic shear zones, the faulting is synchronous with post-26 Ma oblique rifting in the Terror Rift, as indicated by plate motion studies (Granot & Dyment, 2018) and seismic reflection data (Sauli et al., 2021).

7.2. Thermochronological Evidence

Thermochronologic ages collected along vertical profiles or long fault-orthogonal transects can exhibit outlier samples that deviate from regional trends due to differing thermal histories resulting from faulting, heating, or specific landscape evolution processes. In an extensional setting, such as a rift flank, the strain may be accommodated by nearly vertical normal and oblique fault systems, which segment crustal blocks and cause differential exhumation among them (Fitzgerald, 1992; Tron & Brun, 1991). These anomalies closely reflect the structural architecture of the TAM front, where AFT ages near the coastline in piedmont sectors may be older than samples taken at higher elevations far from the coast (Figures 10b–10f), suggesting a regional downfaulting to the east, parallel to the margin. Small discrepancies in age-elevation relationships have been historically detected even in steep vertical profiles, attributed to the motion of faulted blocks. Heating events may occur due to the presence of magmatic intrusions near the sampling locations (e.g., Balestrieri et al., 1997), frictional heating recorded in zircons (e.g., Murakami & Tagami, 2004), or hot fluid circulation (e.g., Wölfler et al., 2010). Additionally, different exhumation styles can lead to local younging trends of thermochronological ages observed at large scales in rift flanks, as a result of the interplay between isostasy and erosion (e.g., Gallagher et al., 1998).

It is noteworthy that the rejuvenation of AFT ages in fault zones compared to the host rock is attributed to thermal events occurring above the partial annealing zone (PAZ) level (60–120°C), which makes the AFT thermochronological system particularly suitable for detecting very shallow crustal processes. In contrast, zircons have frequently been used to detect anomalies related to frictional heating in deeper fault zones (Tagami, 2012), given that the corresponding PAZ closes at approximately 180°C.

7.2.1. Mt. Gauss

On opposite sides of the Mawson Glacier, Mt. Gauss and Mt. Murray share a similar structural setting along the TAM front, as well as a comparable tectonic and landscape evolution history. This is demonstrated by a consistent gradient in age-elevation relationship (AER) (Figure 10b). From the summit of Mt. Gauss to the sample collected at Cape Day, the AER aligns with a rapid Late Eocene exhumation phase, which coincided with significant climate and geomorphic changes, including erosion of warm-based glaciers (He et al., 2021; McKay et al., 2022). Although faults have been identified between the sampling points during field surveys, the dip-slip offset is minimal, and no substantial vertical motions have affected the area. Only the Cape Hickey and Charcot Cove samples along the coast are slightly older than those at the base of the escarpment (Guzzo et al., 2019). The mid-elevation sample along the Mt. Gauss transect (01-01-19VF13), dated 23.9 ± 5.5 Ma and based on seven grains that form a coherent single population ($P = 91.14\%$), is anomalously younger than AFT samples at similar elevations in the southern Victoria Land (SVL).

Considering the age of the AFT data, if the anomaly in the AER were solely the result of faulting, the vertical offset must have occurred after 24 Ma. The scenario of a rapidly exhuming crustal block at the onset of the Miocene does not align with the regional evolution of the TAM (Fitzgerald, 2002). Additionally, large fault surfaces have not been identified either in the field or through remote sensing along the ridge of Mt. Gauss, whereas several tectonic structures have been detected on the escarpment south of Mt. Perseverance (Figure 4a). We also exclude that the observed AFT ages pattern reflects the effect of local isotherm warping due to abrupt paleo-topography. The relative distances between samples, ~700 m (Figure 10a), appear too short to warp the isotherms reproducing such different cooling histories. Moreover, the sampling profile would be misoriented (E-W) respect to the rift flank at the regional scale (N-S). We propose a second hypothesis: that the young AFT ages observed in samples collected from fault damage zones have been reset due to heating associated with a hydrothermal event that coincided with the Oligocene-Miocene activation of faulting along the TAM front.

The lowest sample, 01-01-19VF15, at the time of the hydrothermal event (~23 Ma), was located just above the upper boundary of the unperturbed PAZ, which corresponds to a depth of approximately 2–2.5 km with a geothermal gradient of 30–40°C/km. We suggest that deformation and mesothermal fluid circulation were predominantly surficial, occurring at depths of around 2 km or less. Sample 01-01-19VF15 reflects a unique exhumation history, as deduced from thermal modeling (Figure 11c), which indicates a double peak in the distribution of confined tracks. This observation is consistent with a prolonged stagnation of apatite grains at temperatures corresponding to the PAZ. We simulated this event using a constraint box centered at 23 Ma, within the temperature range of 80–120°C (Figure 11c). The best-fit model reproduced a heating event followed by rapid cooling during the Miocene.

7.2.2. Mt. Perseverance

At Mt. Perseverance (Figures 10e and 10f), the sample 31-12-18VF8, collected at an elevation of 400 m, appears to have been reset by hydrothermal circulation, yielding an age of 23.4 ± 2.1 Ma based on 20 grains ($P = 91.78\%$). This profile is intersected perpendicularly by a set of NE-SW striking faults characterized by dip-slip-to dextral-oblique slip and a set of N-S dip-slip faults (Figure 4a). Samples 31-12-18VF8 and 31-12-18VF4 (Figure 4c) were collected along the NE-SW striking fault planes and exhibit significant alteration, with mineralized veins cutting through them (Figures 4e and 9e, 9f) (Table S4 in Supporting Information S1). In contrast, sample 31-12-18VF5 is situated outside the damage zone (Figure 4c). The N-S striking faults are part of a series of tectonic alignments that extend from the northern side of the Mackay Valley to the outlet of the Fry Glacier. These faults separate the Tripp Island structural high and cut through the lower portion of Mt. Endeavor (Figure 6). The N-S structural trend is parallel to other lineaments, such as the Evans Fault, previously inferred from thermochronological studies (Fitzgerald, 1992), which are consistent with our measured fault plane data.

At Tripp Island, we suggest that the AFT sample (02-01-19VF3) dated at 35.9 ± 3.4 Ma is downfaulted toward the basin approximately ~900 m, based on the elevation difference with the uppermost sample on Mt. Endeavor (02-01-19VF8) (Figure 10d). This thermochronological ages trend could also result from escarpment exhumation by a downwarping model (e.g., Gallagher et al., 1998). Similarly, at Mt. Perseverance (Figure 10f), the cumulative displacement between samples 31-12-18VF7 and 31-12-18VF5 is estimated to be around 700 m, suggesting the lateral continuity of this fault zone (lineaments dashed in Figure 6 between Tripp Is. and Mt. Endeavor).

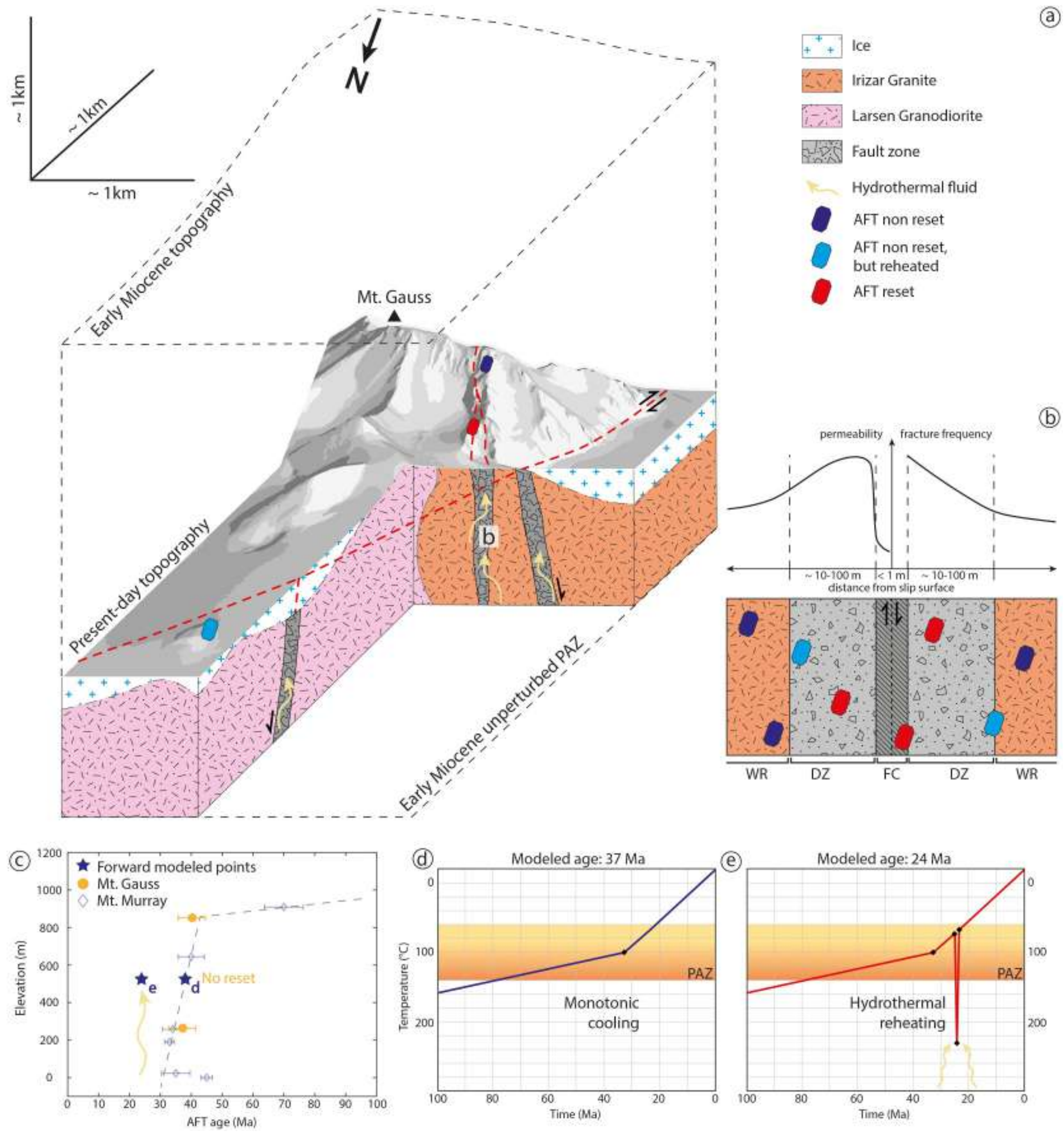

Figure 12. (a) Three-dimensional block diagram illustrating the geological structure of Mt. Gauss. (b) Schematic representation of a fault zone, highlighting its physical properties, such as permeability and fracture frequency, in relation to the potential for apatite resetting. Abbreviations according to Choi et al. (2016): WR, wall-rock; DZ, damage zone; FC, fault core. (c) Apatite fission-track age-elevation relationship for Mt. Gauss. Forward modeling was performed on sample 01-01-19VF13, considering two scenarios: (d) non-reset and (e) reset due to hydrothermal flow. In panel (c) the modeled ages referring to the two different scenarios are shown.

7.2.3. Early Miocene Hydrothermal Reset

Alteration is observed in all samples to different degrees; however, chloritization, carbonatation, and the resetting of apatite grains primarily occur within the damage zone adjacent to the main fault planes. In the proposed scenario, a 3-D conceptual model of Mt. Gauss (Figure 12a) is used to visualize the structurally controlled fluid flow and the selective apatite resetting in zones affected by hydrothermal fluid circulation, mineralization and alteration (Figure 12b). Examining the AER of Mt. Murray and Mt. Gauss at an elevation of approximately 500 m, an AFT sample is expected to have an age of 35–40 Ma (Figure 12c). A simple forward modeling analysis conducted with HeFTy software (Ketcham, 2005) indicates that a monotonic cooling/exhumation model can yield a sample age of 37 Ma (Figure 12d). This model can be further complicated by introducing a phase of rapid reheating above the PAZ temperature (Figure 12e). When temperatures rise to levels consistent with chlorite formation, estimated to be at least ~230°C (Figure 12e), and remain elevated for more than 100 years (as derived from the Arrhenius plot of AFT annealing data; for a comprehensive review, see Hurford, 2019), the previous exhumation history is effectively erased. Consequently, apatite grains record only the last phase of extremely rapid cooling to the surface, after the thermal resetting induced by the mesothermal fluid-rock interaction at ca. 23 Ma. At Mt. Endeavor, apatite grains found in the shear zone (sample 02-01-19VF4) do not show evidence of an early Miocene reset or reheating (Figure 11a). We infer that the deformation along that structure (Figure 7a) occurred at crustal level beneath the PAZ before the Oligocene.

The scenario of formation of breccia bodies at Mt. Gauss (Figures 5d, 8, and 9) may result from one of these two processes: (a) a steam explosion related to the interaction between Ferrar Dolerite sills and the Jurassic water table (e.g., Elliot & Grimes, 2011), or (b) a hydrofracturing process associated with a Cenozoic hydrothermal event. In both hypothesis, a late hydrothermal event led to pseudomorphous replacement of biotite by chlorite and anatase as resulting from removal of cations (e.g., Fe, K, and Ti) during hydrothermal fluid circulation (Parneix et al., 1985). The skeletal texture of titanium oxide mineralization (Figure 8d) suggests an undersaturated environment concerning specific mineral phases. Generally, a hydrothermal environment evolves from a primary mineralization phase to a waning phase, during which there may be secondary enrichment or dissolution of previously precipitated phases. At Mt. Perseverance, open fractures were healed through a multi-stage mineralization process. The observed paragenetic sequence consists of: (a) euhedral quartz, (b) chlorite, (c) quartz overgrowth, and (d) calcite (Figures 9e and 9f). This polyphase mineralization occurred at mesothermal conditions as indicated by the chlorite thermometry, which provided temperature estimates ranging 175–325°C. The precipitation of hydrothermal carbonates is generally linked to CO_2 degassing, as this process effectively removes carbon species from fluids (Zheng, 1990). Additionally, due to the low solubility of calcite at hydrothermal temperatures, CO_2 degassing plays a crucial role in calcite precipitation (Holland & Malinin, 1979; Zheng, 1990). Within the clasts of the Mt. Gauss breccia (Figures 9c and 9d), bastnäsite, a low-temperature REE fluorine carbonate, occurs in association with alkaline volcanism (Zheng & Liu, 2019). Experimental studies indicate that the solubility of LREE such as Ce and La decreases below 300°C (Louvel et al., 2022), with bastnäsite primarily precipitating between 160 and 240°C (Zheng & Liu, 2019). Moreover, an acceptable formation temperature for anatase, the low-temperature TiO_2 polymorph in hydrothermal settings, ranges 200–300°C (e.g., Migaszewski & Galuszka, 2023). These crystallization temperatures align well those obtained with the chlorite thermometry, further confirming the complete reset of the apatite grains during Cenozoic fluid-rock interaction and structurally controlled fluid flow. We therefore infer that the presence of bastnäsite as part of the alteration assemblage indicates hydrothermal fluids likely associated with the Cenozoic McMurdo volcanism. This hypothesis suggests a structural connection with a lithospheric mantle enriched with carbonate-bearing silicate liquids, consistent with the trace element geochemistry of McMurdo alkaline volcanic rocks (Martin et al., 2013; Panter et al., 2018).

7.3. Tectonic and Geodynamic Implications

The onset of the West Antarctic Rift System is believed to have occurred during the late Early Cretaceous (Siddoway et al., 2004), coinciding with the early exhumation of the TAM (Fitzgerald, 2002). Therefore, hydrothermally altered faults such as the those in this study (Olivetti et al., 2018; Storti et al., 2008; Wilson, 1995, 1999) should be viewed as products of a late-stage tectonic reactivation of the rift shoulders. In this context, the TAM rift front, shaped primarily by surface processes and locally supported by dynamic topography (Balestrieri et al., 2020; Faccenna et al., 2008), experienced segmentation due to the onshore partitioning of rifting. As demonstrated by our new AFT data and field surveys, the offsets estimated along dip-slip faults alone cannot fully account for the observed Cenozoic landscape evolution. Only in specific areas, such as the Mt. Perseverance sector, the cumulative offsets of wide fault zones may reach approximately 500–700 m.

7.3.1. Hydrothermal Fluid Circulation and Volcanism

During the Neogene-Quaternary period, extension in western Ross Sea (WRS) was accompanied by the onset of widespread alkaline McMurdo Volcanic Group (Fioraso, Sternai, et al., 2024). This volcanic activity spans the entire length of the Victoria Lands, from seamounts in the Adare Basin to the southern termination of the Victoria Land Basin, where several shield volcanoes are situated (Rocchi & Smellie, 2021; Martin et al., 2021). Partial melting of recycled materials leads to the formation of carbonate-rich silicate liquids in the asthenosphere, which migrate into the lithospheric mantle, resulting in the production of metasomes (Panter et al., 2018; Panter & Martin, 2023). We hypothesize a connection between the advection of hydrothermal fluids in highly fractured fault damage zones and the onset of McMurdo volcanism. The oldest known volcanic products of the McMurdo

Group are ash layers found in the CRP-2/2A core, dated at 24.98 Ma by $^{40}Ar/^{39}Ar$ (McIntosh, 2000) and attributed to Mt. Morning, the oldest recognized eruptive center in the McMurdo province (Smellie & Martin, 2021). Consequently, the hydrothermal activity documented in this study aligns with the early phases of McMurdo volcanism. In this context, the initial magmatic and hydrothermal fluids of the McMurdo Volcanic Group may have exploited crustal discontinuities as preferential pathways, which were reactivated by Cenozoic oblique rifting at the Oligocene-Miocene boundary. The McMurdo volcanism is predominantly focused along intersections of tectonic structures and structural accommodation zones between basins (Ferraccioli et al., 2008; Rocchi et al., 2002; Wilson, 1999), mirroring patterns observed in hydrothermal systems worldwide (Chiodini et al., 2008; Frondini et al., 2008; Hutchinson et al., 2015; Ring et al., 2016; Rowland & Sibson, 2004). However, it is important to note that no volcanic occurrences have been documented in the Convoy Range block, and the nearest evidence of McMurdo volcanism is represented by an intrusion located offshore of Cape Roberts (Hamilton et al., 2001). Thus, the hydrothermal circulation identified in this study may represent the only known magmatic by-product of McMurdo volcanism in this region of the TAM.

On a broader scale, the TAM and western Ross Sea serve as critical zones where deep mantle materials are recycled from older convergence phases and subsequently emitted at the surface as volcanic products and hydrothermal mineralization. The deep crustal structures enhance the connectivity of magmatic-hydrothermal fluids to the surface, which are often enriched in CO_2 and other volatiles dispersed in aqueous solutions. Passive margins and continental rift systems significantly influence the deep carbon cycle (Foley & Fischer, 2017; Lee et al., 2016), CO_2 emissions, and climate over Mesozoic-Cenozoic timescales (Brune et al., 2017). A deep origin for the hydrothermal fluids in the Convoy Range block may provide a link between a major CO_2 sink, such as the paleo-Pacific subduction zone, and volcanogenic emissions along fractured fault zones within the Western Antarctic Rift System, even in the absence of alkaline melts at the surface.

8. Conclusions

We present the first evidence of an early Miocene (∼23 Ma) paleo-hydrothermal system in the Convoy Range block of the Transantarctic Mountains, temporally constrained using thermochronology. Our main findings are as follows:

- Fluid flow is associated with brittle deformation and faulting along N-S and NE-SW striking oblique- and dip-slip normal faults.
- The structural architecture is developed by the onshore propagation of oblique rifting from the NNW-SSE striking right-lateral fault system on the western border of the Victoria Land Basin, which intersects the Transantarctic Mountain rift flank.
- Rock damage due to faulting and hydrofracturing has produced dilational fractures that host mineralized veins. This process has also facilitated fluid-driven alteration processes, such as the propylitization of the granitic host rock. The upward advection of hot fluids locally perturbed the thermal state of the investigated area, suggesting temperatures sufficient to reset the apatite fission-track system.
- Fluid temperatures, estimated via chlorite thermochronometry, range between 175 and 325°C. These estimates have been incorporated into thermochronological modeling to assess the effective resetting of apatite grains.
- The age of the hydrothermal system is consistent with the first occurrence of volcanogenic products in the region, linking fluid circulation and CO_2 degassing with syn-rift melting in the mantle. We propose that the fluids are primarily magmatic-hydrothermal, dissolved in silicate magma, and released from solution during decompression and crystallization.

Conflict of Interest

The authors declare no conflicts of interest relevant to this study.

Data Availability Statement

Data presented in this study including: field site locations (Table S1 in Supporting Information S1), structural measurements (Table S2 in Supporting Information S1), rock samples (Table S3 in Supporting Information S1), chemical microanalysis (Tables S4, S6 and S7 in Supporting Information S1) and fission-track data (Tables S8 and S9 in Supporting Information S1), are available electronically at Zenodo https://doi.org/10.5281/zenodo.

14010414 (Fioraso, Olivetti, et al., 2024). Maps and figures were produced using QGIS and Adobe Illustrator. Structural data were analyzed and plotted using: MATLAB R2022b for pitch Gaussian fit, mplstereonet python package available at https://pypi.org/project/mplstereonet for stereonets, and Daisy3 software (Salvini et al., 1999) for density contour plot in Figure 6.

Acknowledgments

We are grateful to Whitney Behr for editorial handling and to the two anonymous reviewers whose comments helped to improve the manuscript. This work was supported by the Italian Programma Nazionale di Ricerche in Antartide (Grant PNRA 2016/AZ2.05) (coordinated by V. Olivetti). Analyzed samples are stored at the Museo Nazionale dell'Antartide – Siena Section (http://www.mna.it/siena/siena-sede-espositiva); we wish to acknowledge its staff. We are deeply grateful to Silvia Cattò for her assistance in sample preparation and fission-track analysis.

References

Aitken, A. R. A., Li, L., Kulessa, B., Schroeder, D., Jordan, T. A., Whittaker, J. M., et al. (2023). Antarctica sedimentary basins and their influence on ice-sheet dynamics. *Reviews of Geophysics*, *61*(3). https://doi.org/10.1029/2021RG000767

Ault, A. K. (2020). Hematite fault rock thermochronometry and textures inform fault zone processes. *Journal of Structural Geology*, *133*, 104002. https://doi.org/10.1016/j.jsg.2020.104002

Balestrieri, M. L., Bigazzi, G., & Ghezzo, C. (1997). Uplift - Denudation of the transantarctic mountains between the David and the Mariner glaciers, northern Victoria Land (Antarctica): Constraints by apatite fission-track analysis. In *VII international symposium on Antarctic earth sciences, Siena, Italy* (pp. 547–554).

Balestrieri, M. L., Olivetti, V., Rossetti, F., Gautheron, C., Cattò, S., & Zattin, M. (2020). Topography, structural and exhumation history of the Admiralty Mountains region, northern Victoria Land, Antarctica. *Geoscience Frontiers*, *11*(5), 1841–1858. https://doi.org/10.1016/j.gsf.2020.01.018

Bialas, R. W., Buck, W. R., Studinger, M., & Fitzgerald, P. G. (2007). Plateau collapse model for the transantarctic mountains-West Antarctic rift system: Insights from numerical experiments. *Geology*, *35*(8), 687–690. https://doi.org/10.1130/G23825A.1

Bourdelle, F. (2021). Low-temperature chlorite geothermometry and related recent analytical advances: A review. *Minerals*, *11*(2), 130. https://doi.org/10.3390/min11020130

Bourdelle, F., & Cathelineau, M. (2015). Low-temperature chlorite geothermometry: A graphical representation based on a T–R2+ –Si diagram. *European Journal of Mineralogy*, *27*(5), 617–626. https://doi.org/10.1127/ejm/2015/0027-2467

Braun, J. (2018). A review of numerical modeling studies of passive margin escarpments leading to a new analytical expression for the rate of escarpment migration velocity. *Gondwana Research*, *53*, 209–224. https://doi.org/10.1016/j.gr.2017.04.012

Braun, J., & Beaumont, C. (1989). A physical explanation of the relation between flank uplifts and the breakup unconformity at rifted continental margins. *Geology*, *17*(8), 760–764. https://doi.org/10.1130/0091-7613(1989)017<0760:apeotr>2.3.co;2

Braun, J., & van der Beek, P. (2004). Evolution of passive margin escarpments: What can we learn from low-temperature thermochronology? *Journal of Geophysical Research: Earth Surface*, *109*(F4). https://doi.org/10.1029/2004jf000147

Brenn, G. R., Hansen, S. E., & Park, Y. (2017). Variable thermal loading and flexural uplift along the Transantarctic Mountains, Antarctica. *Geology*, *45*(5), 463–466. https://doi.org/10.1130/G38784.1

Brune, S., Kolawole, F., Olive, J. A., Stamps, D. S., Buck, W. R., Buiter, S. J. H., et al. (2023). Geodynamics of continental rift initiation and evolution. *Nature Reviews Earth & Environment*, *4*(4), 235–253. https://doi.org/10.1038/s43017-023-00391-3

Brune, S., Williams, S. E., & Müller, R. D. (2017). Potential links between continental rifting, CO2 degassing and climate change through time. *Nature Geoscience*, *10*(12), 941–946. https://doi.org/10.1038/s41561-017-0003-6

Calzolari, G., Rossetti, F., Ault, A. K., Lucci, F., Olivetti, V., & Nozaem, R. (2018). Hematite (U-Th)/He thermochronometry constrains intraplate strike-slip faulting on the Kuh-e-Faghan Fault, central Iran. *Tectonophysics*, *728–729*, 41–54. https://doi.org/10.1016/j.tecto.2018.01.023

Cande, S. C., & Stock, G. M. (2006). Constraints on the timing of extension in the Northern Basin, Ross Sea. In D. K. Fütterer, D. Damaske, G. Kleinschimdt, H. Miller, & F. Tessensohn (Eds.), *Antarctica*. Springer. https://doi.org/10.1007/3-540-32934-X_40

Cape Roberts Science Team. (2000). Studies from Cape Roberts project initial report on CRP-3, Ross Sea, Antarctica. *Terra Antarctica*, *7*(1–2), 1–209.

Capponi, G., Montomoli, C., Casale, S., & Simonetti, M. (2020). Geology of the northern Convoy Range, Victoria Land, Antarctica. *Journal of Maps*, *16*(2), 702–709. https://doi.org/10.1080/17445647.2020.1822218

Capponi, G., Montomoli, C., Simonetti, M., Salvatore, M. C., Casale, S., Musumeci, G., et al. (2024). A comprehensive 1:250,000 scale geological map of the Convoy Range and Franklin island quadrangles (Victoria Land, Antarctica). *GFT&M*, *16*(1.5), 1–22. https://doi.org/10.3301/gft.2024.05

Chiodini, G., Caliro, S., Cardellini, C., Avino, R., Granieri, D., & Schmidt, A. (2008). Carbon isotopic composition of soil CO2 efflux, a powerful method to discriminate different sources feeding soil CO2 degassing in volcanic-hydrothermal areas. *Earth and Planetary Science Letters*, *274*(3–4), 372–379. https://doi.org/10.1016/j.epsl.2008.07.051

Choi, J. H., Edwards, P., Ko, K., & Kim, Y. S. (2016). Definition and classification of fault damage zones: A review and a new methodological approach. *Earth-Science Reviews*, *152*, 70–87. https://doi.org/10.1016/j.earscirev.2015.11.006

Cianfarra, P., Locatelli, M., Capponi, G., Crispini, L., Rossi, C., Salvini, F., & Federico, L. (2022). Multiple reactivations of the Rennick graben fault system (northern Victoria Land, Antarctica): New evidence from paleostress analysis. *Tectonics*, *41*(6). https://doi.org/10.1029/2021TC007124

Cooper, A. K., Davey, F. J., & Behrendt, J. C. (1991). Structural and depositional controls on Cenozoic and (?) Mesozoic strata beneath the western Ross Sea. In M. R. A. Thomson, J. A. Crame, & J. W. Thomson (Eds.), *Geological evolution of Antarctica* (pp. 279–283). Cambridge University Press.

Cornamusini, G., Zurli, L., Liberato, G. P., Corti, V., Gulbranson, E. L., Perotti, M., & Sandroni, S. (2023). A lithostratigraphic reappraisal of a Permian-Triassic fluvial succession at Allan Hills (Antarctica) and implications for the terrestrial end-Permian extinction event. *Palaeogeography, Palaeoclimatology, Palaeoecology*, *627*, 111741. https://doi.org/10.1016/j.palaeo.2023.111741

Cox, S. C., Smith Lyttle, B., Elkind, S., Smith Siddoway, C., Morin, P., Capponi, G., et al. (2023). A continent-wide detailed geological map dataset of Antarctica. *Scientific Data*, *10*(1), 250. https://doi.org/10.1038/s41597-023-02152-9

Cox, S. C., Turnbull, I. M., Isaac, M. J., Townsend, D. B., & Lyttle, B. S. (2012). *Geology of southern Victoria Land, Antarctica*. GNS Science.

Davey, F. J., Granot, R., Cande, S. C., Stock, J. M., Selvans, M., & Ferraccioli, F. (2016). Synchronous oceanic spreading and continental rifting in West Antarctica. *Geophysical Research Letters*, *43*(12), 6162–6169. https://doi.org/10.1002/2016GL069087

Di Vincenzo, G., Pennacchioni, G., & Bestmann, M. (2019). Exploring the Ar isotope record of an early Miocene pseudotachylyte in an early Oligocene intrusion (Rieserferner pluton, eastern Alps). *Lithos*, *338–339*, 1–17. https://doi.org/10.1016/j.lithos.2019.04.009

Di Vincenzo, G., Rocchi, S., Rossetti, F., & Storti, F. (2004). 40Ar-39Ar dating of pseudotachylytes: The effect of clast-hosted extraneous argon in Cenozoic fault-generated friction melts from the West Antarctic Rift System. *Earth and Planetary Science Letters*, *223*(3–4), 349–364. https://doi.org/10.1016/j.epsl.2004.04.042

Di Vincenzo, G., Rossetti, F., Viti, C., & Balsamo, F. (2013). Constraining the timing of fault reactivation: Eocene coseismic slip along a Late Ordovician ductile shear zone (northern Victoria Land, Antarctica). *Geological Society of America Bulletin*, *125*(3–4), 609–624. https://doi.org/10.1130/B30670.1

Dubbini, M., Cianfarra, P., Casula, G., Capra, A., & Salvini, F. (2010). Active tectonics in northern Victoria Land (Antarctica) inferred from the integration of GPS data and geologic setting. *Journal of Geophysical Research*, *115*(12). https://doi.org/10.1029/2009JB007123

Durkin, K., Day, J. M. D., Panter, K. S., Xu, J. F., & Castillo, P. R. (2023). Petrogenesis of alkaline magmas across a continent to ocean transect, northern Ross Sea, Antarctica. *Chemical Geology*, *641*, 121780. https://doi.org/10.1016/j.chemgeo.2023.121780

Elliot, D. H. (1975). Tectonics of Antarctica: A review. *American Journal of Science*, *275A*, 45–106.

Elliot, D. H. (2013). The geological and tectonic evolution of the transantarctic mountains: A review. *Geological Society Special Publication*, *381*(1), 7–35. https://doi.org/10.1144/SP381.14

Elliot, D. H., & Fleming, T. H. (2021). Ferrar large igneous province: Petrology. In J. L. Smellie, K. S. Panter, & A. Geyer (Eds.), *Volcanism in Antarctica: 200 million years of subduction, rifting and continental break-up*. Geological Society London Memoirs. https://doi.org/10.1144/M55-2018-39

Elliot, D. H., & Grimes, C. G. (2011). Triassic and Jurassic strata at Coombs Hills, south Victoria Land: Stratigraphy, petrology and cross-cutting breccia pipes. *Antarctic Science*, *23*(3), 268–280. https://doi.org/10.1017/S0954102010000994

Elliot, D. H., White, J. D. L., & Fleming, T. H. (2021). Ferrar large igneous province: Volcanology. In J. L. Smellie, K. S. Panter, & A. Geyer (Eds.), *Volcanism in Antarctica: 200 million years of subduction, rifting and continental break-up*. Geological Society London Memoirs. https://doi.org/10.1144/M55-2018-44

Faccenna, C., Rossetti, F., Becker, T. W., Danesi, S., & Morelli, A. (2008). Recent extension driven by mantle upwelling beneath the Admiralty Mountains (East Antarctica). *Tectonics*, *27*(4). https://doi.org/10.1029/2007TC002197

Ferraccioli, F., Armadillo, E., Jordan, T., Bozzo, E., & Corr, H. (2009). Aeromagnetic exploration over the East Antarctic ice sheet: A new view of the Wilkes subglacial basin. *Tectonophysics*, *478*(1–2), 62–77. https://doi.org/10.1016/j.tecto.2009.03.013

Ferraccioli, F., Armadillo, E., Zunino, A., Bozzo, E., Ricchi, S., & Armienti, P. (2008). Magmatic and tectonic patterns over the Northern Victoria Land sector of the Transantarctic Mountains from new aeromagnetic imaging. *Tectonophysics*, *478*(1–2), 43–61. https://doi.org/10.1016/j.tecto.2008.11.028

Fioraso, M., Olivetti, V., Balsamo, F., Rossetti, F., Zattin, M., & Cornamusini, G. (2024). Multi-analytical investigations of hydrothermal activity and faulting in the Convoy Range sector (southern Victoria Land, Antarctica) (Version 1) [Dataset]. *Zenodo*. https://doi.org/10.5281/zenodo.14010414

Fioraso, M., Sternai, P., Olivetti, V., Balestrieri, M. L., Zattin, M., & Cornamusini, G. (2024). Miocene climate cooling and aridification of Antarctica may have enhanced syn-extensional magmatism in the western Ross Sea. *Global and Planetary Change*, *240*, 104538. https://doi.org/10.1016/j.gloplacha.2024.104538

Fitzgerald, P. G. (1992). The transantarctic mountains of southern Victoria Land: The application of apatite fission track analysis to a rift shoulder uplift. *Tectonics*, *11*(3), 634–662. https://doi.org/10.1029/91tc02495

Fitzgerald, P. G. (2002). Tectonics and landscape evolution of the Antarctic plate since the breakup of Gondwana, with an emphasis on the West Antarctic Rift System and the transantarctic mountains. In J. A. Gamble, A. John, D. N. B. Skinner, N. B. David, & S. Henrys (Eds.), *Antarctica at the close of a millennium* (Vol. 35, pp. 453–469). Royal Society of New Zealand Bulletin.

Foley, S. F., & Fischer, T. P. (2017). An essential role for continental rifts and lithosphere in the deep carbon cycle. *Nature Geoscience*, *10*(12), 897–902. https://doi.org/10.1038/s41561-017-0002-7

Frondini, F., Caliro, S., Cardellini, C., Chiodini, G., Morgantini, N., & Parello, F. (2008). Carbon dioxide degassing from Tuscany and northern Latium (Italy). *Global and Planetary Change*, *61*(1–2), 89–102. https://doi.org/10.1016/j.gloplacha.2007.08.009

Galbraith, R. F. (1981). On statistical models for fission track counts. *Mathematical Geology*, *13*(6), 471–488. https://doi.org/10.1007/bf01034498

Gallagher, K., Brown, R., & Johnson, C. (1998). Fission track analysis and its applications to geological problems. *Annual Review of Earth and Planetary Sciences*, *26*(1), 519–572. https://doi.org/10.1146/annurev.earth.26.1.519

Gleadow, A. J. W., & Fitzgerald, P. G. (1987). Uplift history and structure of the transantarctic mountains: New evidence from fission track dating of basement apatites in the Dry Valleys area, southern Victoria Land. *Earth and Planetary Science Letters*, *82*(1–2), 1–14. https://doi.org/10.1016/0012-821x(87)90102-6

Goodge, J. W. (2020). Geological and tectonic evolution of the Transantarctic Mountains, from ancient craton to recent enigma. *Gondwana Research*, *80*, 50–122. https://doi.org/10.1016/j.gr.2019.11.001

Granot, R., & Dyment, J. (2018). Late Cenozoic unification of East and west Antarctica. *Nature Communications*, *9*(1), 3189. https://doi.org/10.1038/s41467-018-05270-w

Gunn, B. M., & Warren, G. (1962). Geology of Victoria Land between the Mawson and Mulock Glaciers. *New Zealand Geological Survey Bulletin*, *71*, 1–157.

Guzzo, G., Cattò, S., Olivetti, V., Zattin, M., Balsamo, F., Balestrieri, M. L., & Rossetti, F. (2019). Thermochronological evolution of transantarctic mountains in the Mt Murray area. Abstract, SGI-SIMP Conference, Parma.

Hamilton, R. J., Luyendyk, B. P., Sorlien, C. C., & Bartek, L. R. (2001). Cenozoic tectonics of the Cape Roberts Rift Basin and transantarctic mountains front, southwestern Ross Sea, Antarctica. *Tectonics*, *20*(3), 325–342. https://doi.org/10.1029/2000TC001218

Hansman, R. J., Albert, R., Gerdes, A., & Ring, U. (2018). Absolute ages of multiple generations of brittle structures by U-Pb dating of calcite. *Geology*, *46*(3), 207–210. https://doi.org/10.1130/G39822.1

Harry, D. L., Anoka, J. L., & Jha, S. (2018). Geodynamic models of the West Antarctic Rift System: Implications for the mantle thermal state. *Geosphere*, *14*(6), 2407–2429. https://doi.org/10.1130/GES01594.1

He, J., Thomson, S. N., Reiners, P. W., Hemming, S. R., & Licht, K. J. (2021). Rapid erosion of the central Transantarctic Mountains at the Eocene-Oligocene transition: Evidence from skewed (U-Th)/He date distributions near Beardmore Glacier. *Earth and Planetary Science Letters*, *567*, 117009. https://doi.org/10.1016/j.epsl.2021.117009

Holland, H. D., & Malinin, S. D. (1979). The solubility and occurrence of non-ore minerals. In H. L. Barnes (Ed.), *Geochemistry of hydrothermal ore deposits* (2nd ed., pp. 461–508). John Wiley and Sons.

Howat, I., Porter, C., Noh, M., Husby, E., Khuvis, S., Danish, E., et al. (2022). The reference elevation model of Antarctica – Mosaics, version 2. *Harvard Dataverse*. https://doi.org/10.7910/DVN/EBW8UC

Huerta, A. D., & Harry, D. L. (2007). The transition from diffuse to focused extension: Modeled evolution of the West Antarctic Rift system. *Earth and Planetary Science Letters*, *255*(1–2), 133–147. https://doi.org/10.1016/j.epsl.2006.12.011

Hurford, A. J. (2019). An historical perspective on fission-track thermochronology. In M. G. Malusà & P. G. Fitzgerald (Eds.), *Fission-track thermochronology and its application to geology*. Springer Textbooks in Earth Sciences, Geography and Environment. https://doi.org/10.1007/978-3-319-89421-8_1

Hutchison, W., Mather, T. A., Pyle, D. M., Biggs, J., & Yirgu, G. (2015). Structural controls on fluid pathways in an active rift system: A case study of the Aluto volcanic complex. *Geosphere*, *11*(3), 542–562. https://doi.org/10.1130/GES01119.1

Jordan, T. A., Riley, T. R., & Siddoway, C. S. (2020). The geological history and evolution of West Antarctica. *Nature Reviews Earth & Environment*, *1*(2), 117–133. https://doi.org/10.1038/s43017-019-0013-6

Ketcham, R. A. (2005). Forward and inverse modeling of low-temperature thermochronometry data. *Reviews in Mineralogy and Geochemistry*, *58*(1), 275–314. https://doi.org/10.2138/rmg.2005.58.11

Ketcham, R. A. (2019). Fission-track annealing: From geologic observations to thermal history modeling. In M. G. Malusà & P. G. Fitzgerald (Eds.), *Fission-track thermochronology and its application to geology*. Springer Textbooks in Earth Sciences, Geography and Environment. https://doi.org/10.1007/978-3-319-89421-8_3

Lee, H., Muirhead, J. D., Fischer, T. P., Ebinger, C. J., Kattenhorn, S. A., Sharp, Z. D., & Kianji, G. (2016). Massive and prolonged deep carbon emissions associated with continental rifting. *Nature Geoscience*, *9*(2), 145–149. https://doi.org/10.1038/ngeo2622

Levy, R. H., Meyers, S. R., Naish, T. R., Golledge, N. R., McKay, R. M., Crampton, J. S., et al. (2019). Antarctic ice-sheet sensitivity to obliquity forcing enhanced through ocean connections. *Nature Geoscience*, *12*(2), 132–137. https://doi.org/10.1038/s41561-018-0284-4

Lisker, F., & Läufer, A. L. (2013). The mesozoic victoria basin: Vanished link between Antarctica and Australia. *Geology*, *41*(10), 1043–1046. https://doi.org/10.1130/G33409.1

Louvel, M., Etschmann, B., Guan, Q., Testemale, D., & Brugger, J. (2022). Carbonate complexation enhances hydrothermal transport of rare earth elements in alkaline fluids. *Nature Communications*, *13*(1), 1456. https://doi.org/10.1038/s41467-022-28943-z

Martin, A. P., & Cooper, A. F. (2010). Post 3.9 Ma fault activity within the West Antarctic rift system: Onshore evidence from Gandalf ridge, Mount Morning eruptive centre, southern Victoria Land, Antarctica. *Antarctic Science*, *22*(5), 513–521. https://doi.org/10.1017/S095410201000026X

Martin, A. P., Cooper, A. F., & Price, R. C. (2013). Petrogenesis of Cenozoic, alkalic volcanic lineages at Mount Morning, West Antarctica and their entrained lithospheric mantle xenoliths: Lithospheric versus asthenospheric mantle sources. *Geochimica et Cosmochimica Acta*, *122*, 127–152. https://doi.org/10.1016/j.gca.2013.08.025

McDermott, R. G., Ault, A. K., & Caine, J. S. (2021). Dating fault damage along the eastern Denali fault zone with hematite (U-Th)/He thermochronometry. *Earth and Planetary Science Letters*, *563*, 116872. https://doi.org/10.1016/j.epsl.2021.116872

McIntosh, W. C. (2000). $^{40}Ar/^{39}Ar$ geochronology of tephra and volcanic clasts in CRP-2A, Victoria Land Basin, Antarctica. *Terra Antarctica*, *7*(4), 621–630.

McKay, R. M., Escutia, C., De Santis, L., Donda, F., Duncan, B., Gohl, K., et al. (2022). Cenozoic history of Antarctic glaciation and climate from onshore and offshore studies. In F. Florindo, M. Siegert, L. De Santis, T. Naish (Eds.), *Antarctic Climate Evolution* (pp. 41–164). Elsevier. https://doi.org/10.1016/b978-0-12-819109-5.00008-6

Migaszewski, Z. M., & Galuszka, A. (2023). Hydrothermal TiO2 polymorphs in a pyrite stratiform deposit: Lessons from a mineralogical and geochemical multiproxy record. *Chemical Geology*, *632*, 121551. https://doi.org/10.1016/j.chemgeo.2023.121551

Milesi, G., Monié, P., Münch, P., Soliva, R., Taillefer, A., Bruguier, O., et al. (2020). Tracking geothermal anomalies along a crustal fault using (U-Th)/He apatite thermochronology and rare-earth element (REE) analyses: The example of the Têt fault (Pyrenees, France). *Solid Earth*, *11*(5), 1747–1771. https://doi.org/10.5194/se-11-1747-2020

Miller, S. R., Fitzgerald, P. G., & Baldwin, S. L. (2010). Cenozoic range-front faulting and development of the Transantarctic Mountains near Cape Surprise, Antarctica: Thermochronologic and geomorphologic constraints. *Tectonics*, *29*(1). https://doi.org/10.1029/2009TC002457

Morlighem, M., Rignot, E., Binder, T., Blankenship, D., Drews, R., Eagles, G., et al. (2020). Deep glacial troughs and stabilizing ridges unveiled beneath the margins of the Antarctic ice sheet. *Nature Geoscience*, *13*(2), 132–137. https://doi.org/10.1038/s41561-019-0510-8

Muirhead, J. D., Kattenhorn, S. A., Lee, H., Mana, S., Turrin, B. D., Fischer, T. P., et al. (2016). Evolution of upper crustal faulting assisted by magmatic volatile release during early-stage continental rift development in the East African Rift. *Geosphere*, *12*(6), 1670–1700. https://doi.org/10.1130/GES01375.1

Murakami, M., Košler, J., Takagi, H., & Tagami, T. (2006). Dating pseudotachylyte of the Asuke Shear Zone using zircon fission-track and U-Pb methods. *Tectonophysics*, *424*(1–2), 99–107. https://doi.org/10.1016/j.tecto.2006.06.006

Murakami, M., & Tagami, T. (2004). Dating pseudotachylyte of the Nojima fault using the zircon fission-track method. *Geophysical Research Letters*, *31*(12). https://doi.org/10.1029/2004GL020211

Nuriel, P., Rosenbaum, G., Zhao, J. X., Feng, Y., Golding, S. D., Villemant, B., & Weinberger, R. (2012). U-Th dating of striated fault planes. *Geology*, *40*(7), 647–650. https://doi.org/10.1130/g32970.1

Olivetti, V., Rossetti, F., Balestrieri, M. L., Pace, D., Cornamusini, G., & Talarico, F. (2018). Variability in uplift, exhumation and crustal deformation along the Transantarctic Mountains front in southern Victoria Land, Antarctica. *Tectonophysics*, *745*, 229–244. https://doi.org/10.1016/j.tecto.2018.08.017

Panter, K. S., Castillo, P., Krans, S., Deering, C., McIntosh, W., Valley, J. W., et al. (2018). Melt origin across a rifted continental margin: A case for subduction-related metasomatic agents in the lithospheric source of alkaline basalt, NW Ross Sea, Antarctica. *Journal of Petrology*, *59*(3), 517–558. https://doi.org/10.1093/petrology/egy036

Panter, K. S., & Martin, A. P. (2023). West Antarctic mantle deduced from mafic magmatism. In A. P. Martin, & W. van der Wall (Eds), *The geochemistry and geophysics of the Antarctic Mantle, Geological Society Memoirs* (Vol. 56(1), pp. 133–149). https://doi.org/10.1144/m56-2021-10

Parneix, J. C., Beaufort, D., Dudoignon, P., & Meunier, A. (1985). Biotite chloritization process in hydrothermally altered granites. *Chemical Geology*, *51*(1–2), 89–101. https://doi.org/10.1016/0009-2541(85)90089-0

Pérez-Gussinyé, M., Collier, J. S., Armitage, J. J., Hopper, J. R., Sun, Z., & Ranero, C. R. (2023). Towards a process-based understanding of rifted continental margins. *Nature Reviews Earth & Environment*, *4*(3), 166–184. https://doi.org/10.1038/s43017-022-00380-y

Prenzel, J., Lisker, F., Balestrieri, M. L., Läufer, A., & Spiegel, C. (2013). The Eisenhower Range, Transantarctic Mountains: Evaluation of qualitative interpretation concepts of thermochronological data. *Chemical Geology*, *352*, 176–187. https://doi.org/10.1016/j.chemgeo.2013.06.005

Prenzel, J., Lisker, F., Monsees, N., Balestrieri, M. L., Läufer, A., & Spiegel, C. (2018). Development and inversion of the mesozoic Victoria basin in the Terra Nova Bay (transantarctic mountains) derived from thermochronological data. *Gondwana Research*, *53*, 110–128. https://doi.org/10.1016/j.gr.2017.04.025

Rilling, S., Mukasa, S., Wilson, T., Lawver, L., & Hall, C. (2009). New determinations of40Ar/39Ar isotopic ages and flow volumes for Cenozoic volcanism in the Terror Rift, Ross Sea, Antarctica. *Journal of Geophysical Research*, *114*(12). https://doi.org/10.1029/2009JB006303

Ring, U., Tonguç Uysal, I., Yüce, G., Ünal-İmer, E., Italiano, F., İmer, A., & Zhao, J. X. (2016). Recent mantle degassing recorded by carbonic spring deposits along sinistral strike-slip faults, south-central Australia. *Earth and Planetary Science Letters*, *454*, 304–318. https://doi.org/10.1016/j.epsl.2016.09.017

Roberts, N. M. W., & Holdsworth, R. E. (2022). Timescales of faulting through calcite geochronology: A review. *Journal of Structural Geology*, *158*, 104578. https://doi.org/10.1016/j.jsg.2022.104578

Rocchi, S., Armienti, P., D'Orazio, M., Tonarini, S., Wijbrans, J. R., & Di Vincenzo, G. (2002). Cenozoic magmatism in the western Ross embayment: Role of mantle plume versus plate dynamics in the development of the West Antarctic Rift System. *Journal of Geophysical Research*, *107*(B9). https://doi.org/10.1029/2001jb000515

Rocchi, S., Di Vincenzo, G., Ghezzo, C., & Nardini, I. (2009). Granite-lamprophyre connection in the latest stages of the early Paleozoic Ross Orogeny (Victoria Land, Antarctica). *Geological Society of America Bulletin*, *121*(5–6), 801–819. https://doi.org/10.1130/B26342.1

Rocchi, S., & Smellie, J. L. (2021). Northern Victoria Land: Petrology. In J. L. Smellie, K. S. Panter, & A. Geyer (Eds.), *Volcanism in Antarctica: 200 million years of subduction, rifting and continental break-up*. Geological Society London Memoirs. https://doi.org/10.6084/m9.figshare.c.5198177

Rossetti, F., Lisker, F., Storti, F., & Läufer, A. L. (2003). Tectonic and denudational history of the Rennick Graben (north Victoria Land): Implications for the evolution of rifting between East and west Antarctica. *Tectonics*, *22*(2). https://doi.org/10.1029/2002TC001416

Rossetti, F., Storti, F., Busetti, M., Lisker, F., di Vincenzo, G., Läufer, A. L., et al. (2006). Eocene initiation of Ross Sea dextral faulting and implications for East Antarctic neotectonics. *Journal of the Geological Society*, *163*(1), 119–126. https://doi.org/10.1144/0016-764905-005

Rowland, J. V., & Sibson, R. H. (2004). Structural controls on hydrothermal flow in a segmented rift system, Taupo Volcanic Zone, New Zealand. *Geofluids*, *4*(4), 259–283. https://doi.org/10.1111/j.1468-8123.2004.00091.x

Salvini, F., Billi, A., & Wise, D. U. (1999). Strike-slip fault-propagation cleavage in carbonate rocks: The Mattinata Fault Zone, southern apennines, Italy. *Journal of Structural Geology*, *21*(12), 1731–1749. https://doi.org/10.1016/s0191-8141(99)00120-0

Salvini, F., Brancolini, G., Busetti, M., Storti, F., Mazzarini, F., & Coren, F. (1997). Cenozoic geodynamics of the Ross Sea region, Antarctica: Crustal extension, intraplate strike-slip faulting, and tectonic inheritance. *Journal of Geophysical Research*, *102*(11), 24669–24696. https://doi.org/10.1029/97jb01643

Sauli, C., Sorlien, C., Busetti, M., De Santis, L., Geletti, R., Wardell, N., & Luyendyk, B. P. (2021). Neogene development of the Terror Rift, western Ross Sea, Antarctica. *Geochemistry, Geophysics, Geosystems*, *22*(3). https://doi.org/10.1029/2020GC009076

Siddoway, C. (2008). Tectonics of the West Antarctic Rift System: New light on the history and dynamics of distributed intracontinental extension. In A. K. Cooper, P. J. Barrett, H. Stagg, E. Storey, & W. Wise (Eds.), *Proceedings of the 10th international symposium on Antarctic earth sciences*. The National Academies Press. https://doi.org/10.3133/of2007-1047.kp09

Siddoway, C. S., Baldwin, S. L., Fitzgerald, P. G., Fanning, C. M., & Luyendyk, B. P. (2004). Ross sea mylonites and the timing of intracontinental extension within the West Antarctic rift system. *Geology*, *32*(1), 57–60. https://doi.org/10.1130/G20005.1

Smellie, J. L., & Martin, A. P. (2021). Erebus volcanic province: Volcanology. In J. L. Smellie, K. S. Panter, & A. Geyer (Eds.), *Volcanism in Antarctica: 200 million years of subduction, rifting and continental break-up*. Geological Society London Memoirs. https://doi.org/10.6084/m9.figshare.c.5332477

Smellie, J. L., & Rocchi, S. (2021). Northern Victoria Land: Volcanology. In J. L. Smellie, K. S. Panter, & A. Geyer (Eds.), *Volcanism in Antarctica: 200 million years of subduction, rifting and continental break-up*. Geological Society London Memoirs. https://doi.org/10.1144/M55-2018-60

Stern, T. A., Baxter, A. K., & Barrett, P. J. (2005). Isostatic rebound due to glacial erosion within the Transantarctic Mountains. *Geology*, *33*(3), 221–224. https://doi.org/10.1130/G21068.1

Storti, F., Balestrieri, M. L., Balsamo, F., & Rossetti, F. (2008). Structural and thermochronological constraints to the evolution of the West Antarctic Rift System in central Victoria Land. *Tectonics*, *27*(4). https://doi.org/10.1029/2006TC002066

Storti, F., Salvini, F., Rossetti, F., & Phipps Morgan, J. (2007). Intraplate termination of transform faulting within the Antarctic continent. *Earth and Planetary Science Letters*, *260*(1–2), 115–126. https://doi.org/10.1016/j.epsl.2007.05.020

Stump, E. (1995). *The Ross orogen of the transantarctic mountains* (p. 284). Cambridge University Press.

Sugden, D., & Denton, G. (2004). Cenozoic landscape evolution of the Convoy Range to Mackay Glacier area, transantartic mountains: Onshore to offshore synthesis. *Geological Society of America Bulletin*, *116*(7–8), 840–857. https://doi.org/10.1130/B25356.1

Sugden, D. E., & Jamieson, S. S. R. (2018). The pre-glacial landscape of Antarctica. *Scottish Geographical Journal*, *134*(3–4), 203–223. https://doi.org/10.1080/14702541.2018.1535090

Tagami, T. (2012). Thermochronological investigation of fault zones. *Tectonophysics*, *538–540*, 67–85. https://doi.org/10.1016/j.tecto.2012.01.032

Tagami, T. (2019). Application of fission-track thermochronology to understand fault zones. In M. G. Malusà & P. G. Fitzgerald (Eds.), *Fission-track thermochronology and its application to geology*. Springer Textbooks in Earth Sciences, Geography and Environment. https://doi.org/10.1007/978-3-319-89421-8_12

Tagami, T., Lal, N., Sorkhabi, R. B., & Nishimura, S. (1988). Fission track thermochronologic analysis of the Ryoke belt and the Median Tectonic Line, southwest Japan. *Journal of Geophysical Research*, *93*(B11), 13705–13715. https://doi.org/10.1029/jb093ib11p13705

Tessensohn, F., Wörnerm, G., Kleinschmidt, G., Henjes-Kunst, F., Fenn, G., & Matzer, S. (1992). The Johnnie Walker: A pre-granite Harbour subvolcanic unit in the Wilson terrane, lower Mawson Glacier, Victoria Land, Antarctica. *Polarforschung*, *60*(2), 91–95.

Tinto, K. J., Padman, L., Siddoway, C. S., Springer, S. R., Fricker, H. A., Das, I., et al. (2019). Ross Ice Shelf response to climate driven by the tectonic imprint on seafloor bathymetry. *Nature Geoscience*, *12*(6), 441–449. https://doi.org/10.1038/s41561-019-0370-2

Tron, V., & Brun, J.-P. (1991). Experiments on oblique rifting in brittle-ductile systems. *Tectonophysics*, *188*(1–2), 71–84. https://doi.org/10.1016/0040-1951(91)90315-j

van Der Beek, P., Cloetingh, S., & Andriessen, P. (1994). Mechanisms of extensional basin formation and vertical motions at rift flanks: Constraints from tectonic modelling and fission-track thermochronology. *Earth and Planetary Science Letters*, *121*(3–4), 417–433. https://doi.org/10.1016/0012-821X(94)90081-7

Vignaroli, G., Balsamo, F., Giordano, G., Rossetti, F., & Storti, F. (2015). Miocene-to-Quaternary oblique rifting signature in the western Ross Sea from fault patterns in the McMurdo volcanic group, north Victoria Land, Antarctica. *Tectonophysics*, *656*, 74–90. https://doi.org/10.1016/j.tecto.2015.05.027

Watanabe, Y., Nakai, S., & Lin, A. (2008). Attempt to determine U-Th ages of calcite veins in the Nojima fault zone, Japan. *Geochemistry Journal*, *42*(6), 507–513. https://doi.org/10.2343/geochemj.42.507

Wildman, M., Cogné, N., & Beucher, R. (2019). Fission-track thermochronology applied to the evolution of passive continental margins. In M. G. Malusà & P. G. Fitzgerald (Eds.), *Fission-track thermochronology and its application to geology*. Springer Textbooks in Earth Sciences, Geography and Environment. https://doi.org/10.1007/978-3-319-89421-8_20

Wilson, D. S., & Luyendyk, B. P. (2009). West antarctic paleotopography estimated at the eocene-oligocene climate transition. *Geophysical Research Letters*, *36*(16). https://doi.org/10.1029/2009GL039297

Wilson, T. J. (1995). Cenozoic transtension along the transantarctic mountains-West Antarctic rift boundary, southern Victoria Land, Antarctica. *Tectonics*, *14*(2), 531–545. https://doi.org/10.1029/94TC02441
Wilson, T. J. (1999). Cenozoic structural segmentation of the Transantarctic Mountains rift flank in southern Victoria Land. *Global and Planetary Change*, *23*(1–4), 105–127. https://doi.org/10.1016/s0921-8181(99)00053-3
Wölfler, A., Kurz, W., Danišík, M., & Rabitsch, R. (2010). Dating of fault zone activity by apatite fission track and apatite (U-Th)/He thermochronometry: A case study from the Lavanttal fault system (eastern Alps). *Terra Nova*, *22*(4), 274–282. https://doi.org/10.1111/j.1365-3121.2010.00943.x
Woolfe, K. J., & Barrett, P. J. (1995). Constraining the devonian to triassic tectonic evolution of the Ross Sea sector. *Terra Antarctica*, *2*(1), 7–21.
Yamada, R., Matsuda, T., & Omura, K. (2007). Apatite and zircon fission-track dating from the Hirabayashi-NIED borehole, Nojima Fault, Japan: Evidence for anomalous heating in fracture zones. *Tectonophysics*, *443*(3–4), 153–160. https://doi.org/10.1016/j.tecto.2007.01.014
Yavuz, F., Kumral, M., Karakaya, N., Karakaya, M. T., & Yildirim, D. K. (2015). A Windows program for chlorite calculation and classification. *Computers & Geosciences*, *81*, 101–113. https://doi.org/10.1016/j.cageo.2015.04.011
Zanchetta, S., D'Adda, P., Zanchi, A., Barberini, V., & Villa, I. M. (2011). Cretaceous-Eocene compression in the central Southern Alps (N Italy) inferred from 40Ar/39Ar dating of pseudotachylytes along regional thrust faults. *Journal of Geodynamics*, *51*(4), 245–263. https://doi.org/10.1016/j.jog.2010.09.004
Zanutta, A., Negusini, M., Vittuari, L., Cianfarra, P., Salvini, F., Mancini, F., et al. (2017). Monitoring geodynamic activity in the Victoria Land, east Antarctica: Evidence from GNSS measurements. *Journal of Geodynamics*, *110*, 31–42. https://doi.org/10.1016/j.jog.2017.07.008
Zheng, X., & Liu, Y. (2019). Mechanisms of element precipitation in carbonatite-related rare-earth element deposits: Evidence from fluid inclusions in the Maoniuping deposit, Sichuan Province, southwestern China. *Ore Geology Reviews*, *107*, 218–238. https://doi.org/10.1016/j.oregeorev.2019.02.021
Zheng, Y.-E. (1990). Carbon-oxygen isotopic covariation in hydrothermal calcite during degassing of CO_2 A quantitative evaluation and application to the Kushikino gold mining area in Japan Model for CO2 degassing. *Mineralium Deposita*, *25*(4). https://doi.org/10.1007/bf00198993
Zurli, L., Liberato, G. P., Perotti, M., Woo, J., Lee, M. J., & Cornamusini, G. (2024). A multi-proxy detrital study from Permian-Triassic fluvial sequences of Victoria Land (Antarctica): Implications for the Gondwanan basin evolution. *Palaeogeography, Palaeoclimatology, Palaeoecology*, *641*, 112113. https://doi.org/10.1016/j.palaeo.2024.112113
Zurli, L., Perotti, M., & Cornamusini, G. (2024b). Composition of Late Paleozoic Ice Age tillites in Victoria Land (Antarctica): Implications for sediment provenance and ice centers extent in southern Gondwana. *Rendiconti Online della Società Geologica Italiana*, *63*, 37–44. https://doi.org/10.3301/ROL.2024.27

References From the Supporting Information

Dunkl, I. (2002). Trackkey: A windows program for calculation and graphical presentation of fission track data. *Computers & Geosciences*, *28*(1), 3–12. https://doi.org/10.1016/S0098-3004(01)00024-3
Gleadow, A. J. W., Belton, D. X., Kohn, B. P., & Brown, R. W. (2002). Fission track dating of phosphate minerals and the thermochronology of apatite. *Reviews in Mineralogy and Geochemistry*, *48*(1), 579–630. https://doi.org/10.2138/rmg.2002.48.16
Hurford, A. J., & Green, P. F. (1983). The zeta age calibration of fission-track dating. *Isotope Geoscience*, *1*, 285–317. https://doi.org/10.1016/s0009-2541(83)80026-6